Draft version March 24, 2016
Preprint typeset using LaTeX style emulateapj v. 01/23/15

arXiv:1602.07704v2 [astro-ph.CO] 23 Mar 2016

SEARCHING FOR BULK MOTIONS IN THE INTRACLUSTER MEDIUM OF MASSIVE, MERGING CLUSTERS WITH *CHANDRA* CCD DATA

Ang Liu[1,2], Heng Yu[1,3], Paolo Tozzi[4,1] and Zong-Hong Zhu[1]

Draft version March 24, 2016

ABSTRACT

We search for bulk motions in the intracluster medium (ICM) of massive clusters showing evidence of an ongoing or recent major merger with spatially resolved spectroscopy in *Chandra* CCD data. We identify a sample of 6 merging clusters with >150 ks *Chandra* exposure in the redshift range $0.1 < z < 0.3$. By performing X-ray spectral analysis of projected ICM regions selected according to their surface brightness, we obtain the projected redshift maps for all of these clusters. After performing a robust analysis of the statistical and systematic uncertainties in the measured X-ray redshift z_X, we check whether or not the global z_X distribution differs from that expected when the ICM is at rest. We find evidence of significant bulk motions at more than 3σ in A2142 and A115, and less than 2σ in A2034 and A520. Focusing on single regions, we identify significant localized velocity differences in all of the merging clusters. We also perform the same analysis on two relaxed clusters with no signatures of recent mergers, finding no signs of bulk motions, as expected. Our results indicate that deep *Chandra* CCD data enable us to identify the presence of bulk motions at the level of $v_{\rm BM} > 1000$ km s^{-1} in the ICM of massive merging clusters at $0.1 < z < 0.3$. Although the CCD spectral resolution is not sufficient for a detailed analysis of the ICM dynamics, *Chandra* CCD data constitute a key diagnostic tool complementing X-ray bolometers on board future X-ray missions.

Subject headings: galaxies: clusters: intracluster medium — X-rays: galaxies: clusters

1. INTRODUCTION

Clusters of galaxies are the largest virialized systems in the universe, and the strong interplay between their baryonic and dark components is such that they are at the crossroads between astrophysics and cosmology. It is widely accepted that clusters form in a hierarchical manner from a primordial density perturbation field, and evolve through the accretion and merging of other virialized halos. In particular, merging between halos frequently happens at early epochs and still occurs today. Such merging processes strongly affect the dynamic structure of clusters, often producing bulk motions in the hot intracluster medium (hereafter ICM). On one hand, ICM bulk motions could potentially provide an important diagnostic of the formation and evolution of clusters. On the other hand, the ICM velocity field is extremely difficult to measure with our present facilities, and, more importantly, since measurements of the cluster properties rely on the assumption of hydrostatic equilibrium, unnoticed bulk motions may significantly affect observables such as total mass proxies and baryon mass fractions (Nagai et al. 2013; Nelson et al. 2014). Consequently, this will also affects studies of the formation of large-scale structure and constraints on cosmological parameters (see Allen et al. 2011, for a review).

Bremsstrahlung emission from the optically thin, hot ICM is observed in the X-ray band, and it constitutes a powerful diagnostics of the thermodynamics of the ICM itself, allowing one to measure the temperature and density of the emitting gas. In addition, thanks to the almost perfect collisional equilibrium, the measurement of the line emission from highly ionized heavy elements constitutes a direct probe of the metal content of the ICM. Merging processes can introduce several clear signatures in the ICM, such as the irregular distribution of the X-ray surface brightness, the inhomogeneous distribution of temperatures, and fluctuations in the ICM velocity field, as already mentioned. These signatures last for one or more dynamical times until the relaxation processes bring the ICM back to hydrostatic equilibrium. The surface brightness distribution and temperature map of the ICM of massive clusters is routinely obtained from X-ray imaging and spatially resolved spectroscopy. The direct observation of bulk motion instead presents several difficulties. In some rare cases, the bulk motion velocities can be estimated indirectly via the properties of the bow shock resulting from a tangential merging process, as in the well-known cases of the Bullet cluster (Markevitch et al. 2002), A2146 (Russell et al. 2011), A520 (Markevitch et al. 2005), and a few others. The turbulence expected as a result of the stirring of the ICM during the merger process can be investigated by Doppler line broadening in the high-resolution spectra obtained with the Reflection Grating Spectrometer on board *XMM-Newton*. However, only upper limits in the range 200–600 km s^{-1} have been obtained, and only for the central regions (Sanders et al. 2010; Pinto et al. 2015). Alternatively, the power spectrum of the velocities can be inferred from the power spectrum of the gas density fluctuations (Zhuravleva et al. 2014).

A straightforward approach is to directly measure the ICM velocity field along the line of sight through the Doppler shift of its emission lines. The most prominent emission line of the ICM X-ray spectra is the ubiquitous K-shell line complex of H-like and He-like iron in the 6.7–6.9 keV rest frame, originally detected by Mitchell et al. (1976). Many other emission lines, including the L-shell from iron and α-element transitions, may also be found, particularly in the soft energy range (0.5–2.0 keV). However, the Kα iron complex is the only one

[1] Department of Astronomy, Beijing Normal University, Beijing 100875, China; yuheng@bnu.edu.cn, zhuzh@bnu.edu.cn
[2] Homer L. Dodge Department of Physics and Astronomy, University of Oklahoma, Norman, OK 73019, USA
[3] Dipartimento di Fisica, Universitá di Torino, Via P. Giuria 1, I-10125 Torino, Italy
[4] INAF – Osservatorio Astrofisico di Arcetri, Largo E. Fermi, I-50122 Firenze, Italy

which is detectable in any cluster observed with a total number of net counts as low as $\sim$ 1000 in the entire X-ray band (see Yu et al. 2011). In fact, iron line emission has been identified in X-ray clusters as distant as $z \sim 1.5$ (Rosati et al. 2004, 2009; Stanford et al. 2005; Tozzi et al. 2013), although the detection may be challenging at $z > 1.5$ (see, e.g., Tozzi et al. 2015).

Despite this, applying this method to the measurement of ICM bulk motions is extremely challenging. The typical gas velocity of 1000 km s^{-1} (Nagai et al. 2003) expected in major mergers corresponds only to a ~20 eV shift of the Kα iron line complex in the 6.7–6.9 keV rest frame. Such a shift is below the CCD energy resolution of *XMM-Newton*/EPIC, *Chandra*/ACIS, and *Suzaku*/XIS (~100 eV). This constitutes a major obstacle to the direct measurement of the line-of-sight ICM velocity field. Despite these difficulties, there are a few works that have successfully achieved detections of bulk motions in massive, nearby clusters using spatially resolved spectral analysis of CCD data. The first successful detection was made in the Centaurus cluster with *ASCA* (Dupke & Bregman 2001a). The typical bulk motion velocity was constrained to $(2.4 \pm 0.1) \times 10^3$ km s^{-1}, and was eventually confirmed by *Chandra* data (Dupke & Bregman 2006). Another case is the Perseus cluster, which was also found to present ICM bulk motions by ASCA (Dupke & Bregman 2001b). The first systematic search for ICM bulk motions was performed by Dupke & Bregman (2005) with *ASCA*, but only 2 out of 12 low-redshift ($z < 0.13$) clusters showed reliable signatures of bulk motions. In addition, a significant velocity difference of $(5.9 \pm 1.6) \times 10^3$ km s^{-1} between two regions of Abell 576 was found by combining *Chandra* and *XMM-Newton* data (Dupke et al. 2007).

Thanks to its lower background at high energies, *Suzaku*/XIS has been used to search for radial bulk motions in the ICM through X-ray redshift measurements. However, only upper limits of the order of 2000 km s^{-1} are derived for AWM7, Abell 2319, and Coma (Sato et al. 2008, 2011; Sugawara et al. 2009, respectively), and ~300 km s^{-1} for Centaurus (Tamura et al. 2014). Only in one case (Abell 2256; Tamura et al. 2011) has a robust detection of a bulk motion of 1500 ± 300 km s^{-1} has been found. Recently, Ota & Yoshida (2015) searched for gas bulk motion in eight nearby clusters with *Suzaku*, finding signs of large bulk velocity in excess of their uncertainties in only two of them (Abell 2029 and Abell 2255). Despite the low background of *Suzaku*/XIS, its low angular resolution is a major limiting factor for this investigation. Surprisingly, *Chandra ACIS* has not been used often for these studies, despite its high angular resolution which allows one to focus on smaller regions and, in principle, to detect more efficiently the effects of bulk motions.

Recently, we proposed a strategy to search for bulk motion in the ICM along the line of sight by performing spatially resolved spectral analysis in *Chandra* CCD data of the so-called Bullet cluster 1E0657-56 (Liu et al. 2015). This case turned out to be particularly challenging due to the extremely high temperatures, which make the iron emission line complex less prominent, and the fact that the merger is occurring in the plane of the sky. Nevertheless, we were able to find tantalizing $\sim 2\sigma$ evidence for a bulk motion of the significant mass of ICM in two regions near the center. This is consistent with the picture where the ICM is pushed perpendicularly to the bullet trail due to the extremely large pressure reached when crossing the main cluster center. Future missions carrying X-ray bolometers (e.g., Astro-H; Takahashi et al. 2014) may be able to confirm or rule out this result (see the recent simulations by Biffi et al. 2013).

In this work, we intend to apply our technique to a sample of massive, merging clusters imaged by *Chandra*. Our goal is to investigate whether ICM bulk motions in medium-redshift (z ~ 0.1–0.3) clusters classified as major mergers can be detected in *Chandra* ACIS data. We also try to provide robust estimators of the ICM bulk motions whenever possible, such as the global rms velocity difference across the cluster $v_{\rm BM}$ and the maximum velocity difference measured across the cluster $\Delta v_{\rm max}$. We also aim to provide a qualitative description of the dynamical status of the ICM in single clusters through visual inspection of the redshift map, in order to exploit the angular resolution of *Chandra*.

The paper is organized as follows. In Section 2, we describe the sample selection. In Section 3, we describe the X-ray data reduction and analysis, including a brief description of the strategy already presented in Liu et al. (2015). In Section 4, we present results for the single clusters, while in Section 5 we synthesize the results for the entire sample. In Section 6, we discuss future prospects for improvements in this field. Finally, in Section 7, we summarize our conclusions. Throughout this paper, we adopt the 7 years *WMAP* cosmology, with $\Omega_{\rm m}$= 0.272, Ω_Λ = 0.728, and H_0 = 70.4 km s^{-1} Mpc^{-1} (Komatsu et al. 2011). Quoted error bars always correspond to a 1σ confidence level.

2. SAMPLE SELECTION

We search the *Chandra* data archive for clusters classified as mergers based on their X-ray morphology, radio diffuse emission, and/or galaxy dynamics, in the redshift range $0.1 < z < 0.3$. Since our goal is to perform spatially resolved spectral analyses with high signal-to-noise ratios (S/Ns), we require long exposure times. We fix the threshold for the minimum total exposure to 150 ks on ACIS-I or ACIS-S. The signatures of an occurring, or impending, major merger, are a clear bimodal or multiple stucture in the redshift distribution of the member galaxies, a strongly disturbed appearance in the X-ray surface brightness, or the presence of a radio halo or radio relic. We found six clusters showing at least one of these prominent properties. The clusters are listed in Table 1 in order of increasing optical redshift, together with *Chandra* Obsid and total exposure time (after data reduction).

A2142 is classified as a merger on the basis of its X-ray morphology (Parekh et al. 2015) and the presence of a radio halo (Cuciti et al. 2015). A2034 is classified as a merger on the basis of a shock visible in the X-ray surface brightness (Owers et al. 2014). Abell 115 has a clear bimodal appearance in the X-ray and has a radio relic (Cuciti et al. 2015). A520 shows a clear radio halo (Cuciti et al. 2015) and a clearly disturbed appearance in the X-ray band. 1RXS J0603.3+4214 has a clear bimodal structure and a bright, peculiar radio relic, known as the "Toothbrush" (van Weeren et al. 2012). A2146 shows a prominent bow shock in the *Chandra* X-ray image, indicating a violent merger analogous to the more famous Bullet cluster 1E0657-56, which was the subject of our first investigation of ICM bulk motion (Liu et al. 2015). The properties of each cluster will be discussed in more details in Section 4.

As an immediate check of the robustness of our analysis, we also select two relaxed clusters in the same redshift range and with comparable exposure depth. The two clusters in this control sample are Abell 1689 and Abell 1835, and are listed in Table 2. Clearly, we do not expect to detect any departure from statistical noise in the $z_{\rm X}$ distribution of these relaxed

TABLE 1
SAMPLE OF MERGING CLUSTERS AND CORRESPONDING *Chandra* OBSERVATIONS USED IN THIS WORK.

Cluster Name	Optical Redshift	ObsID	Total Exposure (ks)
A2142	0.090(1)	ACIS-S: 15186-16564-16565	155.1
A2034	0.113(2)	ACIS-I: 7695-2204-12885 13192-12886-13193	254.5
A115	0.197(3)	ACIS-I: 13458-13459-15578-15581	310.6
A520	0.203(4)	ACIS-I: 4215-9424-9425-9426-9430	516.4
1RXS J0603.3+4214	0.225(5)	ACIS-I:15171-15172-15323	235.9
A2146	0.234(6)	ACIS-I: 12245-12246-12247-13020 13021-13023-13120-13138	375.3

[a]The observing mode is VFAINT for all the ObsID. The exposure times in the fourth column correspond to the effective values after data reduction. Optical redshift references: (1)Parekh et al. (2015), (2)Muriel & Coenda (2014), (3)Hiroi et al. (2013), (4)Cassano et al. (2013), (5)van Weeren et al. (2012), (6)Piffaretti et al. (2011).

TABLE 2
RELAXED CLUSTERS AND CORRESPONDING *Chandra* OBSERVATIONS USED IN THIS WORK.

Cluster Name	Optical Redshift	ObsID	Total Exposure (ks)
A1689	0.183(7)	ACIS-I: 5004-6930-7289-7701	151.3
A1835	0.252(8)	ACIS-I: 6880-6881-7370	193.7

[a]The observing mode is VFAINT for all the ObsID. The exposure times in the fourth column correspond to the effective values after data reduction. Optical redshift reference: (7)Hiroi et al. (2013), (8)Girardi et al. (2014).

clusters.

3. DATA REDUCTION AND ANALYSIS

3.1. *Data reduction*

The *Chandra* observations used in this work are listed in Table 1 and 2. All of the observations were taken in VFAINT mode with ACIS-I, except in the case of A2142 which was observed with ACIS-S. The data are reduced using the *ciao* software (version 4.7) with CALDB 4.6.8. The detailed data reduction procedure has been described in Liu et al. (2015). The area of the clusters used in this analysis is defined as the circular region which provides the maximum S/N in the 0.5–10 keV band once the unresolved sources are removed. Point sources are detected by running the *wavdetect* task and are then visually inspected, in particular, to remove those deeply embedded in the strong ICM emission. The background files are extracted from a series of circular regions as far as possible from the cluster area, but still on the solid angle defined by the overlap of all of the Obsids. To define the cluster subregions, we apply the contour binning technique (Sanders 2006) within the maximum S/N circle. Regions are identified simply on the basis of the surface brightness contours in the 0.5–10 keV band image. To make sure that each region can be used to constrain the X-ray redshift with comparable accuracy, we set a criterion in terms of S/N in the 0.5–10 keV band in each region. Clearly, this criterion does not take into account the expected gradient in the iron abundance, which significantly affects the visibility of the iron emission line complex. We set this threshold to S/N> 140, except in the case of Abell 2146 where we choose a weaker constraint of S/N> 100 due to the relatively lower number of counts. The S/N threshold and the number of regions selected in each cluster are listed in Table 3. For each region, the spectrum is extracted from the merged event file after the removal of unresolved sources, while the calibration files (response matrix files, RMF, and ancillary response files, ARF) are generated independently for each ObsID and then combined by weighting them by the corresponding exposure times. In this way, we keep track of all the differences in the ACIS effective area among the different regions in the detector and among the ObsIDs taken at different epochs.

TABLE 3
THE MINIMUM S/N REQUIRED IN EACH REGION AND THE NUMBER OF REGIONS SELECTED FOR SPECTRAL ANALYSIS IN EACH CLUSTER.

Cluster Name	Minimum S/N (0.5–10 keV)	Number of Regions
A2142	140	52
A2034	140	14
A115	140	18
A520	140	20
1RXS J0603.3+4214	140	9
A2146	100	19
A1689	140	10
A1835	140	11

3.2. *Spectral analysis*

In this work, we use the same analysis strategy presented in Liu et al. (2015) to measure the projected X-ray redshift z_X in each region and estimate the total (statistical and systematic) uncertainty. Our analysis is optimized on the basis of the spectral simulations shown in Liu et al. (2015). Here, we simply recall the relevant aspects of the adopted spectral analysis.

The spectra are analyzed using *Xspec* v12.8.2 (Arnaud 1996). To successfully model the X-ray emission, we use two `mekal` plasma emission models (Mewe et al. 1985, 1986; Liedahl et al. 1995) that include thermal bremsstrahlung and line emission, with abundances measured relative to the solar values of Asplund et al. (2005) in which Fe/H = 3.6×10^{-5}. During the fit, the redshift parameters of the two thermal components are always linked together, while the two temperatures and abundances are left as free parameters.

The main advantage in using a double-temperature thermal spectrum is reducing the possible bias in the measurement of the iron line centroid due to the presence of unnoticed ther-

mal structure along the line of sight. As a matter of fact, different temperature components above 3 keV are not detectable, and a single-temperature thermal component would return an excellent fit even in the presence of widely different temperatures (see Mazzotta et al. 2004). However, in Liu et al. (2015), using spectral simulations we showed that the use of two components provides better results for the measurement of the actual redshift of the ICM, while the temperature structure, which is not our main interest here, is essentially left unconstrained. Clearly, this also introduces a larger systematic uncertainty associated with the temperature structure, which is carefully evaluated during our analysis, as explained below.

Galactic absorption is described by the model `tbabs` (Wilms et al. 2000). The central values of the Galactic HI column density NH_{Gal} are based on Kalberla et al. (2005). We conservatively allow NH_{Gal} to vary by an interval of $\sim 10\%$ around the central value. This has a small effects since our best-fit z_X are obtained from spectral fits in the hard (2–10 keV) band, which is only marginally affected by the Galactic absorption. Cash statistics (Cash 1979) are applied to the unbinned source and background spectra in order to exploit the full spectral resolution of the ACIS-I and ACIS-S CCD. Cash statistics are preferred for faint spectra with respect to the canonical χ^2 analysis of binned data (Nousek & Shue 1989). To avoid local minima, we repeat the fit several times before and after running the `steppar` command on all of the free parameters, particularly on the redshift, with a step of $\delta z = 10^{-4}$. Finally, the plots of ΔC_{stat} versus redshift are visually inspected to investigate whether or not there are other possible minima around the best-fit values (see also Yu et al. 2011), which could indicate a noisy spectrum and therefore an unreliable best-fit value for z_X. We decide to conservatively exclude all of the results with a secondary minimum closer than $\Delta C = 6.6$, which corresponds to a formal 99% confidence level for one free parameter.

Our reference spectral analysis consists of two steps. As the first step, we fit the spectra in the 2–10 keV energy range to obtain the best-fit redshift. We choose to use only the 2–10 keV energy range to minimize the effects of the presence of low-temperature components on the centroid of the iron line emission complex. This conservative choice is also supported by the spectral simulations we presented in Liu et al. (2015). For each region, we produce a plot showing the ΔC_{stat} value versus the redshift, obtained by varying the redshift parameter and marginalizing the fit with respect to the other parameters. The minimum is generally well defined and roughly symmetric, and therefore provides a robust estimate of the statistical uncertainty.

As a second step, we carefully take into account the systematic uncertainties on redshift due to the unknown thermal structure of the ICM. We conservatively consider all of the possible temperature distributions of the ICM by setting a four-dimensional grid of spectral parameters, namely, temperature and abundance of the two thermal components T_1, T_2, Z_1, and Z_2. The steps of the grid are typically 0.5 keV for the temperature and 0.05 for the metal abundance. Clearly, only a subgrid of temperature and abundance values should be taken into account, since some combination of them provides an unacceptable fit. To efficiently select the subgrid, we make use of the full 0.5–10 keV energy range in order to exploit the complete information on the thermal structure and the chemical composition. Therefore, for each region, we measure the best-fit redshift in the full 0.5–10 keV band leaving all of the parameters free, and collect the absolute minimum C_{min}. Then, we select all of the sets of values on the grid that provide a best fit close enough to the absolute best fit. The criterion we adopt is given by $\Delta C_{stat} \equiv C_{stat} - C_{min} < 4.72$, which corresponds to a 1σ confidence level for four free parameters. By applying the criterion $\Delta C_{stat} < 4.72$ for the fits performed in the full 0.5-10 keV band, we select a subgrid of T_1, T_2, Z_1 and Z_2 values statistically compatible within $1\,\sigma$ with the spectrum observed in each region. Then, we run the spectral fit on the subgrid, but focusing again in the 2.0–10 keV band only, and measure a set of best-fit z_X values corresponding to the subgrid parameters. The distribution of z_X obtained in this manner is used to derive a redshift range defined by the upper and lower 90% percentiles of the z_X distribution on the grid, and thus the systematic uncertainties on redshift. Since the systematic uncertainty σ_{syst} is due to the degeneracy of the temperature values, we assume that it is uncorrelated to the statistical error σ_{stat}. Therefore, we compute the total 1σ uncertainty as $\sigma_{tot} = \sqrt{\sigma^2_{stat} + \sigma^2_{syst}}$. We do not consider other relevant sources of systematic errors. Systematics related to calibration issues or the time dependence of the gain are kept under control with a direct check on the fluorescent lines of Au Lα and Ni Kα, which are prominent in the ACIS-I background spectrum at 7.5 and 9.7 keV, respectively. Typically, uncertainties introduced by calibration variation (as a function of position on the CCD or as a function of the observation period) on the merged spectrum of each region correspond to errors ~ 5 times smaller than the typical total uncertainty on z_X (see Liu et al. 2015). Having assessed that gain-calibration does not significantly affect our conclusions, we do not perform a full treatment of the gain-calibration uncertainties in ACIS-I data.

Results are presented in the form of redshift maps and significance maps. In particular, in the significance maps, we combine the information included in the best-fit redshift and the corresponding total error by showing $(z_X - \langle z_X \rangle)/\sigma_{tot}$, where $\langle z_X \rangle$ is the average z_X found across the analyzed regions for which we have a reliable spectral fit. Significant (larger than 2σ) deviations in the redshift map are thus visible as bright blue and bright red regions. The complete spectral results for all of the clusters are also presented in the appendix, where the best-fit redshifts and the corresponding lower and upper statistical and systematic error bars are listed for each region of each cluster (values are rounded to the fourth decimal digit).

3.3. *ICM dynamical analysis*

In this section, we describe how we use the results of the spatially resolved spectral analysis to investigate and possibly characterize the presence of bulk motions in the ICM of each cluster. The first check, analogous to what we did in Liu et al. (2015), is to perform a simple χ^2 test on the distribution of z_X under the assumption of a unique value for the ICM redshift. Therefore, we compute $\chi^2 \equiv \Sigma(z_X - \langle z_X \rangle)^2/\sigma^2_{tot}$ and, assuming $N_{reg} - 1$ degrees of freedom (dof), where N_{reg} is the number of selected regions, we evaluate the probability of being inconsistent with the constant redshift hypothesis. To account for the small differences in the lower and upper error bars, we use the corresponding total error for z_X values lower or higher than $\langle z_X \rangle$.

We also compute the typical bulk motion velocity as the excess of the redshift fluctuations with respect to the statistical and systematic noise. To do that, we simply compute the total root mean square deviation of z_X with respect to the mean,

defined as $\sigma^2_{\rm rms} \equiv \Sigma(z_{\rm X} - \langle z_{\rm X}\rangle)^2$, and compare it to the average uncertainty $\langle\sigma_{\rm tot}\rangle = \Sigma\sigma_{\rm tot}/N_{\rm reg}$ (where we use the average value of the lower and upper error bars when they differ). The average excess, which can be ascribed to bulk motions, is computed as $\sigma^2_{\rm BM} = \sigma^2_{\rm rms} - \langle\sigma^2_{\rm tot}\rangle$. Therefore, the bulk motion velocity averaged over the region included in the maximum S/N radius is finally estimated as $v_{\rm BM} = c \times \sigma_{\rm BM}/(1 + \langle z\rangle)$. The error on $v_{\rm BM}$ is estimated as $\sqrt{2}$ times the total error on the mean. Moreover, in those cases where there is some evidence of bulk motions in the ICM, we also provide the value of the maximum velocity difference $\Delta v_{\rm max}$ found across all of the regions with a reliable spectral fit.

We visually inspect the histogram distribution of $z_{\rm X}$ and the redshift and significance maps to infer information on the dynamical status of the ICM. This was done in Liu et al. (2015) for the Bullet cluster, where the two regions with a maximally different redshift are found to be aligned along the bullet trail. We tentatively interpreted them as two regions pushed in opposite directions and perpendicularly to the direction of the bullet at velocities $\sim$5–6 $\times 10^3$ km s^{-1} with respect to the average cluster redshift. Clearly, it is not always possible to draw simple pictures like this one. However, we try to achieve a simple qualitative classification as pre-merger, ongoing, or post-merger according to whether we can clearly identify two well-defined halos with distinct redshift or a few scattered regions with different redshift. Along this same line, clusters with disturbed surface brightness but no signs of bulk motion may be described as post-merger, a phase in which the bulk motions created by the merger already evolved toward a turbulent velocity field with velocity values below the sensitivity achievable in our data. As previously discussed, the regime of evolved merger, when most of the initial kinetic energy due to the merger evolved into a turbulent velocity field of a few $\times$100 km s^{-1}, can be probed only with the much higher spectral resolution of X-ray bolometers.

4. RESULTS ON INDIVIDUAL CLUSTERS

In this section, we show the results of our analysis. For each of the clusters, we measure the best-fit redshift in all of the selected regions, and hence obtain the redshift map and the significance map as defined in Section 3.2. We also measure the global redshift $z_{\rm Xtot}$, which is defined as the best-fit redshift of the total emission of the cluster within the maximum S/N circle. This value corresponds to the emission-weighted average redshift of the ICM, which in principle may differ significantly from the simple average redshift among the regions $\langle z\rangle$. The statistical significance of the presence of bulk motions is evaluated in each case. Whenever possible, we estimate the typical velocity of the bulk motion $v_{\rm BM}$ and the maximum velocity difference $\Delta v_{\rm max}$. Moreover, for each cluster, we provide a short summary of the available literature concerning their dynamical status.

4.1. *Abell 2142*

Abell 2142 has already been identified as a merger cluster already on the basis of *ROSAT* observations (Henry & Briel 1996), and more recently has been classified as "non-relaxed" on the basis of the X-ray morphology obtained with *Chandra* data by Parekh et al. (2015). The two cold fronts, identified in the northwest and southeast regions, clearly separate cooler gas ($kT \sim$ 7–9 keV) from hotter ($kT >$ 12 keV; Markevitch et al. 2000), making it a promising target to investigate the onset of Kelvin-Helmholtz instabilities at the cold fronts. Evidence of dynamical substructure was also found with optical spectroscopy of the member galaxies (Oegerle et al. 1995). Interestingly, the presence of a narrow-angle tailed radio galaxy may be explained by significant bulk motions in the ICM, as suggested by the statistical analysis of Bliton et al. (1998). Finally, Cuciti et al. (2015) reported A2142 to have a radio halo.

We use the three most recent observation with *Chandra* ACIS-S for a total of 155.1 ks, as listed in Table 1, while we discard two older observations with ACIS-I (ObsID 5005 and 7692). This choice will minimize the difference in calibration between ObsID. The total number of net counts in the 0.5–10 keV band within a circle of 3 arcmin in the merged image is about 10^6. This makes A2142 an ideal target for our analysis, with 52 potentially useful regions for spatially resolved spectral analysis. The best-fit redshift obtained by fitting the total X-ray emission within 3 arcmin is $z_{\rm Xtot} = 0.0852^{+0.0012}_{-0.0009}$. To evaluate the systematic uncertainty on $z_{\rm X}$, we consider a temperature range from 3 to 16 keV to explore the temperature structure of the ICM, despite the fact that the projected temperature shows only a moderate range from 8 to 12 keV. Metal abundances are mildly scattered around $Z = 0.45 Z_\odot$ in the units provided by Asplund et al. (2005), nevertheless we consider a wide range $0.15 < Z/Z_\odot < 1.5$ in order to account for possible large fluctuations. In 5 regions, we find that the X-ray spectral analysis does not provide a reliable value of $z_{\rm X}$, and therefore we use only 47 regions. The best-fit $z_{\rm X}$ of the regions used in our analysis with the corresponding statistical and systematic errors are listed in Table 5. The average redshift is $\langle z_{\rm X}\rangle = 0.0855$, which is almost coincident with the global, emission-weighted redshift $z_{\rm Xtot}$.

The hypothesis of a constant redshift is rejected at more than 3σ, with a $\chi^2 = 88.02$ for 46 dof, as listed in Table 4. However, the histogram distribution of $z_{\rm X}$ (see Figure 1) clearly shows that the evidence of bulk motions comes from three regions (region 2, 8, and 50) maximally distant from the average redshift. The rest of the $z_{\rm X}$ values are distributed according to a Gaussian slightly narrower than the Gaussian whose variance is the average $\sigma^2_{\rm tot}$. This is expected since we assumed a very conservative estimate for $\sigma_{\rm tot}$. The projected X-ray redshift map and significance map are shown in Figure 2. We measure $v_{\rm BM} = 1400 \pm 300$ km s^{-1} for the average bulk motion velocity in the ICM of A2142 within a radius of 3 arcmin. Excluding the three extreme $z_{\rm X}$ regions, we are able to establish a hard upper limit of $v_{\rm BM} < 1450$ km s^{-1}. This result is consistent with the *Suzaku* X-ray spectral analysis by Ota & Yoshida (2015), which provided $\Delta v < 4200$ km s^{-1}. However, thanks to the *Chandra* angular resolution, we find that region 50 is redshifted with respect to the average velocity by 5000 ± 1500 km s^{-1}, while the contiguous regions 2 and 8 are blueshifted by 7400 ± 2200 km s^{-1}. In particular, we can interpret region 50 as being dominated by a significant amount of ICM mass pushed at high velocity as a result of the ongoing merger. The two blueshifted regions can be tentatively associated with some rotation of the ICM. We note that, given the small field of view of the ACIS-S detector, we repeated the spectral analysis with a different choice of background, finding the same statistical results. Therefore, our conclusions are not affected by uncertainties in the background, despite the fact that the cluster emission covers almost the entire ACIS-S field of view.

To summarize, as in the case of the Bullet cluster (Liu et al. 2015), the evidence of bulk motions is coming from a few re-

gions with an extreme redshift difference with respect to the mean after a very conservative selection of reliable spectra and an accurate estimate of the total uncertainty on z_X. This may suggest that the cluster is a post-merger or caught in a stage where the shocks have developed since $\sim$ 1 dynamical time or more and the velocity field of the ICM still shows a few regions with large velocities with respect to the velocity of the center of mass. The interpretation in terms of ICM dynamics is nevertheless still very hard, and a significantly higher spectral resolution with the same angular resolution is needed before the actual velocity field of the ICM can be accurately measured.

4.2. *Abell 2034*

Abell 2034, at redshift $z_{opt} = 0.113$ (Muriel & Coenda 2014), shows many signatures typically associated with merging clusters, from a radio relic near the position of a discontinuity in the X-ray surface brightness, to significant heating of the ICM above its equilibrium temperature, and a significant offset of the cD galaxy from the centroid of the X-ray emission (Kempner & Sarazin 2001; Kempner et al. 2003; Giovannini et al. 2009; van Weeren et al. 2011). In a recent detailed study by Owers et al. (2014) using a deep *Chandra* observation of 250 ks, a shock with a Mach number of 1.59±0.06, corresponding to a shock velocity of ~2000 km s^{-1}, was clearly observed. Combining *Chandra* data with spectroscopic observations for 328 spectroscopically confirmed member galaxies, they show the presence of a substructure located at the front edge of the shock and that the merger is proceeding along a north–south direction with an inclination angle of $\sim 23^\circ$ with respect to the plane of the sky. The cluster is included in the sample of the Merging Cluster Collaboration.[5]

We use *Chandra* ACIS-I observations for a total of 254.5 ks. The total number of net counts in the 0.5–10 keV band is 2.66×10^5 within a circle of 3 arcmin in the merged image. We select 14 ICM regions for redshift analysis, but we obtained reliable spectral fits only in 11 out of 14. We find $z_{Xtot} = 0.1124^{+0.0039}_{-0.0044}$, which is in very good agreement with z_{opt} and $\langle z_X \rangle = 0.1122$. To evaluate the systematic uncertainties on z_X, we consider a temperature and abundance range of 6–12 keV and 0.2–0.8 $Z_\odot$, respectively. The best-fit z_X of the 11 regions used in our analysis with corresponding errors are listed in Table 6. The histogram distribution of z_X shows that most of the best-fit z_X values are approximately distributed as a Gaussian, with the exception of two high-redshift values (see Figure 3). However, due to the estimated uncertainties, the probability of a uniform redshift distribution across the ICM is still high at the 24% level ($\chi^2 = 12.70$ for 10 dof), which implies no significant detection (less than 2σ) of global bulk motions. Formally, we measure an average bulk motion of $v_{BM} = 1700 \pm 840$ km s^{-1}. In addition, the projected redshift map shows that the two high-redshift regions 4 and 9 are contiguous (see Figure 4, lower panels), which can be interpreted as an enhanced likelihood of a redshift difference between the diffuse emission in the north and the main halo. The average redshift of regions 4 and 9 is 0.1310, while that of the other regions is 0.1081. This implies a velocity difference of $\Delta v_{max} = 6200 \pm 3300$ km s^{-1}. The presence of two distinct halos with different redshift may suggest a classification as a pre-merger. Due to the presence of a well-developed shock, this cluster may be caught in the early stages of the merger process, in agreement with the conclusion of Owers et al. (2014), who estimate that the merger is observed only ~0.3 Gyr after core-passage.

[5] http://www.mergingclustercollaboration.org/

4.3. *Abell 115*

Abell 115 has been classified as a merger on the basis of its double X-ray morphology (Forman et al. 1981). The ICM thermal structure is best described by two halos that host a cool core with significantly hotter gas between and around them, suggesting that the system is in an advanced stage of merging, despite the fact that no shock front has been found in this region (Shibata et al. 1999; Gutierrez & Krawczynski 2005). A dynamical analysis based on 88 cluster member spectra (Barrena et al. 2007) shows a line-of-sight velocity difference of 1646 km s^{-1} between the northern and southern subclusters at a projected separation of 0.89 Mpc. In addition, Barrena et al. (2007) interpret the system as a pre-merger based on the location of the BCGs being consistent with the peaks in the X-ray surface brightness distribution. Diffuse radio emission north of the cluster has been found by Govoni et al. (2001) with a 1.4 GHz VLA observation and interpreted as a radio relic that may be associated with the ongoing merger. Abell 115 is also included in the Merging Cluster Collaboration sample.

We used 4 ACIS-I contiguous-in-time observations for a total of 310.6 ks. The total number of counts in the 0.5–10 keV band within a circle of 5.2 arcmin in the merged image is 2.88×10^5. This allows us to obtain 18 useful regions for spectral analysis. Our spatially resolved spectroscopic analysis provides us with reliable z_X only in 12 regions out of 18. The average redshift $\langle z_X \rangle = 0.1979$ is in good agreement with $z_{opt} = 0.197$ (Hiroi et al. 2013) while the global redshift $z_{Xtot} = 0.1892^{+0.003}_{-0.004}$ is significantly lower. To evaluate systematic uncertainties on z_X, we consider temperature and abundance ranges of 2–12 keV and 0.2–0.9 $Z_\odot$, respectively. The best-fit z_X of the 12 regions used in our analysis with corresponding errors are listed in Table 7.

The hypothesis of a constant redshift across the 12 regions is rejected at more than 3σ ($\chi^2 = 30.4$ for 11 dof). The histogram distribution of z_X (see Figure 5) shows the presence of two regions significantly above and below the central value. We measure an average bulk motion velocity of $v_{BM} = 4600 \pm 1100$ km s^{-1}.

Visual inspection of the redshift and significance maps (see Figure 6, lower panels) allows us to identify three main regions with compatible redshift. We first isolate regions belonging to the northern (regions 0, 1, 2, 4, and 10) and southern (3, 6, 11, 17, and 15) clumps. We find a redshift difference that corresponds to about 1σ, and is therefore consistent with having the same redshift. Formally, translated into a velocity difference, this would imply a relative velocity of 3300 ± 3200 km s^{-1}. If we consider instead regions 12 and 14, then we find an average redshift of 0.1634, corresponding to a velocity difference of 8600 ± 3000 km s^{-1} with respect to the bulk of the ICM. We note that this is also the gas that is found to be significantly hotter (at least by a factor of two, as verified in the projected temperature map not discussed here), and therefore it is likely to be heated and violently displaced by the ongoing merger. This is consistent with a substantial amount of the shocked gas being compressed between the two halos and pushed toward the observer, with the two halos having a minimum in the velocity difference. Therefore, we conclude that A115 is caught in the early phase of the merging process, with the two ICM halos still well separated.

4.4. *Abell 520*

Abell 520, at $z_{opt} = 0.203$ (Cassano et al. 2013), was found to host a radio halo elongated in the NE-SW direction, corresponding to the apparent merger axis (Giovannini et al. 1999; Govoni et al. 2001). Its X-ray morphology and the optical spectroscopy suggest a disturbed dynamical state (Govoni et al. 2001; Proust et al. 2000, respectively). Despite the recent in-depth studies (Mahdavi et al. 2007; Girardi et al. 2008), the detailed structure of the merger of Abell 520 is still unclear. However, a prominent bow shock with $M = 2.1^{+0.4}_{-0.3}$ has been identified thanks to *Chandra* data analysis (Markevitch et al. 2005). Abell 115 is also included in the Merging Cluster Collaboration sample.

A520 has the longest *Chandra* ACIS-I exposure for a total of 516.4 ks. The number of net counts in the 0.5–10 keV band in the merged image is 3.36×10^5 in a circle of 3.2 arcmin radius. The best-fit redshift from the global emission is $z_{Xtot} = 0.2082^{+0.0046}_{-0.0049}$. To estimate the systematic uncertainty on z_X, we consider ranges of 3–15 keV and 0.2–1 $Z_\odot$ for temperature and abundance, respectively.

We discard only two regions that do not provide reliable redshifts. Therefore, we base our analysis on 18 regions, whose best-fit z_X and associated errors are listed in Table 8. The average redshift among those regions is $\langle z_X \rangle = 0.2083$, in good agreement with z_{Xtot} and z_{opt}. The hypothesis of a constant redshift is rejected at an ~87% confidence level ($\chi^2 = 23.4$ for 17 dof), which is therefore less than 2σ. We find v_{BM}~1800 ± 900 km s^{-1}. This is mostly contributed by the presence of blueshifted regions, mostly in the central 1 arcmin, and the surrounding higher-redshift regions, as can be seen by comparing the histogram distribution (see Figure 7) with the redshift and significance maps (see Figure 8). If we compute the difference between the two sets of regions with comparable redshifts, then we find $\Delta v_{max} = 5900 \pm 4000$ km s^{-1}. The overall redshift map suggests a merger with a halo moving toward the observer that was caught shortly after the first pericentric passage.

4.5. *1RXS J0603.3+4214*

At redshift $z_{opt} = 0.225$ (van Weeren et al. 2012), 1RXS J0603.3+4214 (the "Toothbrush" cluster) was discovered in the radio band thanks to its prominent linear radio relic and radio halo plus several additional features which suggest that this is a complex merger. Simulations also show that the merger might be a triple process: in addition to northern and southern subclusters with similar mass, there might be another smaller subcluster infalling in the south (Brüggen et al. 2012). Measurement of the radio spectral index allowed van Weeren et al. (2012) to constrain the merger Mach number to be in the range 3.3–4.6. However, X-ray observation by *XMM-Newton* returned a Mach number of <2 (Ogrean et al. 2013), which is inconsistent with the radio constraints. 1RXS J0603.3+4214 is also included in the Merging Cluster Collaboration sample

We use three *Chandra* ACIS-I observations for a total of 235.9 ks. The total number of counts in the 0.5–10 keV band within a circle of 3.5arcmin is 1.74×10^5 in the merged image. To evaluate the systematic uncertainty on z_X, we consider ranges of 8–16 keV and 0.3–0.8 $Z_\odot$ for the temperature and abundance, respectively. We are able to obtain reliable spectral fits in 8 out of the 9 regions originally considered for analysis. The best-fit z_X and corresponding errors are listed in Table 9. The average redshift across the regions is $\langle z \rangle = 0.2303$, which is in good agreement with $z_{Xtot} = 0.2316^{+0.0029}_{-0.0033}$ and in reasonable agreement with z_{opt}. The hypothesis of a constant redshift is acceptable ($\chi^2 = 8.7$ for 7 dof), as also shown in Figure 9 by the histogram distribution of the best-fit z_X values. The upper limit to the average bulk motion velocity is $v_{BM} < 2100$ km s^{-1}. However, there is a significant uniform gradient in the best-fit redshift from the northern clump (high-z) to the southern clump (low-z; see Figure10), which corresponds to a maximum difference of ~0.0295 ± 0.0115, or a maximum velocity difference of $\Delta v_{max} \sim 7200 \pm 2800$ km s^{-1}. On the basis of these results, this cluster can be classified as a pre-merger.

4.6. *Abell 2146*

Despite the lack of diffuse radio emission, A2146 is classified as an extreme binary, head-on cluster merger in Mann & Ebeling (2012). A deep *Chandra* study reveled the presence of two shock fronts with Mach numbers of $M = 2.2 \pm 0.8$ and $M \sim 1.7 \pm 0.3$ (Russell et al. 2010). Using the radial velocity of BCGs in the subcluster and the main cluster, Canning et al. (2012) find that the merger axis has an angle of 17° with respect to the plane of the sky. Based on these properties and its appearance in the X-ray, Abell 2146 is often compared to the Bullet cluster.

We use observations with *Chandra* ACIS-I for a total of 375.3 ks, as listed in Table 1. For simplicity, we do not consider observations with ACIS-S for a total of 45 ks in order to retain uniform calibration throughout our analysis, given the smaller amount of observing time contributed by the ACIS-S exposures. The total number of net counts in the 0.5-10 keV band within a circle of 3.6 arcmin is about 1.99×10^5. The best-fit redshift obtained by fitting the total X-ray emission is $z_{Xtot} = 0.2310^{+0.0022}_{-0.0010}$. Measured temperatures range from the inner ~3 keV to the outer ~8 keV in our analysis of the temperature structure (not reported in this work). To evaluate the systematic uncertainty on z_X, we consider ranges from 1 to 12 keV and 0.15 to 1.5 $Z/Z_\odot$ to explore the temperature and metal abundance throughout the ICM, respectively.

We are able to obtain a reliable spectral fit in 17 out of the 19 regions originally selected in the X-ray image. The best-fit z_X of the regions used in our analysis, along with their corresponding statistical and systematic errors, are listed in Table 10. The average redshift across the region is $\langle z_X \rangle = 0.2338$, which is consistent with z_{Xtot} within 1σ. We find $\chi^2 = 19.68$ for 16 dof, as listed in Table 4, which is pretty much consistent with a constant redshift across the ICM. The histogram distribution of z_X, shown in Figure 11, is consistent with a Gaussian dominated by noise and shows no clear evidence of bulk motions. The average bulk motion is formally $v_{BM} = 480 \pm 490$ km s^{-1}. The projected X-ray redshift map and significance map are shown in Figure 12. The maximum redshift difference is $\Delta v_{max} = 8200 \pm 3600$ km s^{-1} and is obtained between two distinct regions with homogeneous redshift: the "bullet" and its trail, along the direction of the merger, which are blueshifted with respect to the average redshift, and all of the surrounding ICM emission, which is redshifted. Despite the low S/N, the redshift map depicts a clear dynamical situation where the central ICM is dominated by a halo moving toward the observer, while the larger scale emission has, on average, a larger redshift. This provides support for the presence of bulk motions that are still dominated by the infall velocity of the merging halos.

4.7. *Abell 1689*

Abell 1689 is a typical relaxed cluster at $z \sim 0.183$ (Hiroi et al. 2013). We reduced and analyzed four ACIS-I observations for a total of 151.3 ks (see Table 2). The total number of net counts in the 0.5–10 keV band within a circle of 1 arcmin is about 1.86×10^5 in the ACIS-I merged image. The best-fit redshift obtained fitting the total X-ray emission is $z_{\rm Xtot} = 0.1814^{+0.0028}_{-0.0008}$. To evaluate the systematic uncertainty on $z_{\rm X}$, we consider ranges from 5 to 15 keV and 0.3 to 0.9 $Z/Z_\odot$ to explore the temperature and metal abundance throughout the ICM, respectively.

We are able to obtain a reliable spectral fit in all 10 of the regions originally selected in the X-ray image. The best-fit $z_{\rm X}$ of the regions used in our analysis with the corresponding statistical and systematic errors are listed in Table 11. The average redshift across the region is $\langle z_{\rm X} \rangle = 0.1814$. The histogram distribution of $z_{\rm X}$, shown in Figure 13, is consistent with a Gaussian distribution whose σ is the average statistical error on $z_{\rm X}$. We find $\chi^2 = 9.31$ for 9 dof, as listed in Table 4. Therefore, we do not find any hint of bulk motion, as expected, and find a hard upper limit of $v_{\rm BM} < 1600$ km s^{-1}.

4.8. *Abell 1835*

Abell 1835 is a relaxed cluster at $z \sim 0.234$ (Girardi et al. 2014). We reduced and analyzed three ACIS-I observations for a total of 193.7 ks (see Table 2). The total number of net counts in the 0.5–10 keV band within a circle of 1 arcmin is about 2.33×10^5 in the ACIS-I merged data. The best-fit redshift obtained while fitting the total X-ray emission is $z_{\rm Xtot} = 0.2478^{+0.0021}_{-0.0012}$, which is significantly larger than the optical value. To evaluate the systematic uncertainty on $z_{\rm X}$ we consider ranges from 4 to 14 keV and 0.2 to 0.8 $Z/Z_\odot$ to explore the temperature and metal abundance throughout the ICM, respectively.

We are able to obtain a reliable spectral fit in all 11 of the regions originally selected in the X-ray image. The best-fit $z_{\rm X}$ of the regions used in our analysis with the corresponding statistical and systematic errors are listed in Table 12. The average redshift across the region is $\langle z_{\rm X} \rangle = 0.2483$. The histogram distribution of $z_{\rm X}$, shown in Figure 15, is consistent with a Gaussian distribution whose σ is the average statistical error on $z_{\rm X}$. We find $\chi^2 = 11.5$ for 10 dof, as listed in Table 4. Therefore, we do not find any hint of bulk motion, as expected, and find a hard upper limit of $v_{\rm BM} < 1350$ km s^{-1}.

5. STATISTICAL PROPERTIES OF THE CLUSTER SAMPLE

In Figure 17, we summarize our results, showing the χ^2 values versus the dof for all of the clusters analyzed in this work and listed in Table 4. Comparison with the lines corresponding to the 1, 2, and 3σ confidence levels shows that, in general, merging clusters always have a larger probability of showing bulk motions in their ICM, but only in two cases do we have a statistical significance larger than 3σ. In two cases, instead, the probability is less than 2σ. Finally, in the last two cases, the global χ^2 is not significantly different from that of the two relaxed clusters, which show no signs of bulk motions. Globally, the merging cluster sample always shows a larger probability of hosting bulk motions, but it is hard to reach definitive conclusions in single cases.

However, we note that the analysis based simply on the χ^2 including all of the ICM regions tends to dilute the signal, since the majority of the ICM regions are expected to show no significant bulk motions. In fact, the bulk motion signal is created by only a few, large masses of ICM displaced at large velocities during the merger, and, in addition, can be partially erased by projection effects. On the bright side, our global evaluation of bulk motion is free from the "look-elsewhere effect" (Lyons 2008). We conclude that, under our most conservative assumptions, only a fraction of the major mergers shows unambiguous signatures of bulk motions in the *Chandra* CCD data. Specifically, we measure $v_{\rm BM} = 1400 \pm 300$ and 4600 ± 1100 km s^{-1} in A2142 and A115, respectively. In A2034 and A520 we find $v_{\rm BM} = 1700 \pm 840$ and 1800 ± 900 km s^{-1}, respectively, although this measurement is not significant (less then 2σ). In the cases of 1RXS J0603.3+4214 and A2146, we find hard (corresponding to 3σ) upper limit of 2100 and $\sim$1500 km s^{-1}, respectively. These limits are similar to those found for the two relaxed clusters A1689 and A1835, where we find $v_{\rm BM} < 1600$ and $v_{\rm BM} < 1350$ km s^{-1}, respectively.

Local velocity differences between ICM regions may achieve much larger values with corresponding larger errors. In the eighth column of Table 4, we list the values of $\Delta v_{\rm max}$ found by identifying the ICM regions (or groups of regions) with the largest difference in $z_{\rm X}$. Clearly, this does not constitute a detection of bulk motion, however, it does provide a rough estimate of the maximum velocity difference we can have across the ICM in our data.

Visual inspection of the redshift and significance maps also allows us to provide a rough classification in terms of pre-merger or ongoing/post-merger. The first case is when two comparable-mass halos are about to begin a head-on merger with large speed along the line of sight, so that in the redshift map the two halos appear to have clearly distinct average redshifts (see, for example, the case of 1RXS J0603.3+4214). The ongoing or post-merger case is when shocks in the ICM are clearly present and the first pericentric passage is recent (i.e., it happened less than one dynamical time ago, see A2034 and A115). Given the uncertainties on the bulk motion velocity, we are not able to explore the regime where the residual kinetic energy of the merger event has already decreased to a more diffuse and chaotic turbulent velocity field of the order of few $\times$100 km s^{-1}. Our qualitative classification is also provided in the last columns of Table 4.

6. DISCUSSION AND FUTURE PROSPECTS

In this work, we use the same conservative approach that we adopted in Liu et al. (2015), where we explored the presence of bulk motions in the ICM of 1E0657-56. In particular, when estimating the statistical significance of bulk motions, we used five conservative assumptions.

1 We considered only the Fe line emission in the hard band. The use of the soft band would have significantly reduced the statistical error on $z_{\rm X}$, particulary for the cold regions. However, since, in principle, gas with different temperatures can have different positions along the line of sight and different velocities, this may introduce a source of scatter in $z_{\rm X}$ which is hard to control.

2 We computed the total error on $z_{\rm X}$ in each region, summing in quadrature the statistical error and the 90% percentile of the $z_{\rm X}$ distribution obtained by imposing a varying thermal structure in the ICM. This systematic component is often smaller than, or at best comparable to, the statistical component. The systematic component is likely to be slightly overestimated, as we can verify by comparing the $\sigma_{\rm rms}$ of the $z_{\rm X}$ distribution with the average total error $\langle \sigma_{\rm tot} \rangle$.

TABLE 4
THE RESULTS OF THE χ^2 TEST ON THE DISTRIBUTION OF REDSHIFT OF THE CLUSTERS, AND CORRESPONDING CONSTRAINTS ON v_{BM} AND Δv_{max} IN km s^{-1}.

Cluster Name	z_{Xtot}	$\langle z_X \rangle$	Degrees of Freedom ($N_{reg}-1$)	χ^2	Prob of BM	v_{BM} km s^{-1}	Δv_{max} km s^{-1}	Classification
A2142	$0.0852^{+0.0012}_{-0.0009}$	0.0855	46	88.02	99.98%	1400 ± 300	7400 ± 2200	post-merger
A2034	$0.1124^{+0.0039}_{-0.0044}$	0.1122	10	12.70	76%	1700 ± 840	6200 ± 3300	pre/ongoing merger
A115	$0.1892^{+0.0030}_{-0.0040}$	0.1979	11	30.4	99.9%	4600 ± 1100	8600 ± 3000	pre/ongoing merger
A520	$0.2082^{+0.0046}_{-0.0049}$	0.2083	17	23.4	86%	1800 ± 900	5900 ± 4000	post-merger
1RXS J0603.3+4214	$0.2316^{+0.0029}_{-0.0033}$	0.2303	7	8.6	72%	< 2100	7200 ± 2800	pre-merger
A2146	$0.2310^{+0.0022}_{-0.0010}$	0.2338	16	19.68	77%	480 ± 490	8200 ± 3600	pre/ongoing merger
A1689	$0.1814^{+0.0028}_{-0.0008}$	0.1814	9	9.3	59%	< 1600	4600 ± 3000	relaxed
A1835[a]	$0.2478^{+0.0021}_{-0.0012}$	0.2483	10	11.5	38%	< 1350	4200 ± 2600	relaxed

[a]This information is combined with visual inspection of the redshift maps to obtain the qualitative classification listed in the last column.

3 We discarded all of the regions where the best-fit redshift is not identified clearly, rejecting all of the spectra where the C_{stat} versus redshift plot shows a secondary minimum at a distance $\Delta C_{stat} < 6.6$ from the absolute minimum.

4 Although the signature of bulk motion is presumably confined to a few, largely discrepant regions, we evaluate the statistical significance with a simple χ^2 test on all of the regions. This of course would dilute the effect, but provides a robust evaluation of the actual presence of bulk motions completely free from the "look-elsewhere effect" (Lyons 2008).

5 We use information from the spatial distribution of z_X only to provide a qualitative description of the possible dynamical status of the cluster, and not to reinforce the statistical significance of the z_X fluctuations. In practice, we do not redefine regions to merge them together according to their z_X value, a procedure that would reduce the statistical uncertainty on the final z_X maps.

Given our extremely conservative approach, we only hit the tip of the iceberg for signatures of bulk motions in *Chandra* CCD data. At the same time, our results show both the difficulty in measuring bulk motions and also the widespread presence of bulk motions in massive, head-on mergers.

Based on these tantalizing but promising results, in the near future we plan to relax some of these constraints. In particular, we will include soft-band spectral information and quantitatively investigate the spatial correlation of the z_X fluctuations, possibly merging projected ICM regions that have similar redshifts on the basis of the spectral analysis and surface brightness features. In addition, we can also combine X-ray spectrally resolved analyses with dynamical studies based on the optical redshift distribution of the member galaxies. We are currently applying the caustic method (Diaferio 1999; Diaferio et al. 2005; Serra & Diaferio 2013; Yu et al. 2015) to a few nearby, massive clusters in the Abell cluster catalog (Abell et al. 1989) with the aim of carefully comparing the optical dynamical structure to the X-ray morphology and spatially resolved spectral analysis (Yu et al. 2016, in preparation).

Clearly, any improvement that may be achieved with current facilities is limited by the modest spectral resolution. In particular, the inevitable superposition of ICM massive regions with different redshifts along the line of sight heavily blurs the redshift map. Sometimes the presence of more than one minima in the CCD spectra may be interpreted, in principle, as the superposition of two ICM regions moving at different redshift. However, it is impossible to reach this kind of conclusion using the current coarse spectral resolution. In the near future, the X-ray bolometer on board Astro-H (Takahashi et al. 2014) will provide ICM spectra with very high resolution, so that the velocity regime probed in the ICM will reach few ×100 km s^{-1} as opposed to the current limit of ∼2000 km s^{-1}. However, the lack of adequate spatial resolution will still make the *Chandra* data a crucial complementary source of information for exploring the ICM dynamics in the coming years.

7. CONCLUSIONS

We search for bulk motions in the ICM in a sample of six clusters at $0.1 < z < 0.3$ classified as massive mergers on the basis or their X-ray morphology, diffuse radio emission, or dynamical optical substructure, plus two relaxed clusters. By performing spatially resolved spectral analyses on *Chandra* CCD data, we obtain the distribution of the redshift z_X across their ICM after a careful and extremely conservative evaluation of the total error on each z_X value. We accurately investigate the distribution of z_X, the z_X map, and finally obtain a robust estimate of bulk motions in the ICM. Considering the global distribution of z_X across the ICM, our analysis shows that for two of the six merging clusters, there is significant evidence of bulk motions at more than 3σ at the level of $v_{BM} = 1400 \pm 300$ and 4600 ± 1100 km s^{-1} in A2142 and A115, respectively. We also obtain measurements at lower significance (less than 2σ) of $v_{BM} = 1700 \pm 840$ and 1800 ± 900 km s^{-1} in A2034 and A520, respectively. Finally, for two clusters (1RXS J0603.3+4214 and A2146), the global analysis of the z_X distribution is not significantly different from that of two relaxed clusters (A1689 and A1835), where we do not find any signs of bulk motion, as expected.

Eventually, we consider specific regions by combining the z_X distribution with the redshift maps, and we are able to identify regions that show relevant bulk motion velocities in all of the merger clusters. We identify local velocity differences between ICM regions ranging from 5900 to 8600 km s^{-1}, with typical uncertainties of 30%–50%. Whenever possible, we use the spatial distribution of z_X to infer a qualitative description of the dynamical status of the clusters, tentatively classifying them as pre-merger, ongoing, or post-merger. Our results are summarized in Table 4.

We conclude that *Chandra* data can be successfully used to detect ICM bulk motions in massive merging clusters at $0.1 < z < 0.3$. Unfortunately, the CCD coarse spectral resolution makes it impossible to provide a meaningful reconstruction of the velocity field of the ICM in single clusters.

However, as soon as high-resolution, spatially resolved X-ray spectroscopy is available, the ICM dynamics will become a key diagnostic for understanding the dynamics of whole clusters, the physics of the ICM itself, for achieving accurate measurement of the total mass, and, ultimately, for performing accurate cosmological tests based on cluster abundances. We are currently planning a refined strategy to carefully relax some of our assumptions, and may reach a lower velocity regime with current CCD data. The hard limit imposed by the spectral resolution can be partially overcome by near-future X-ray bolometers. However, due to the low angular resolution of X-ray bolometers, *Chandra* data will be a key complementary probe for ICM dynamics in the coming years.

This work was supported by the Chinese Ministry of Science and Technology National Basic Science Program (Project 973) under grants No.2012CB821804 and 2014CB845806, the Strategic Priority Research Program "The Emergence of Cosmological Structure" of the Chinese Academy of Sciences (No. XDB09000000), the National Natural Science Foundation of China under grants Nos. 11373014, 11073005, and 11403002, and the Fundamental Research Funds for the Central Universities and Scientific Research Foundation of Beijing Normal University. P.T. is supported by the Recruitment Program of High-end Foreign Experts and he gratefully acknowledges the hospitality of Beijing Normal University. A.L. is supported by NSF grant AST-1413056.

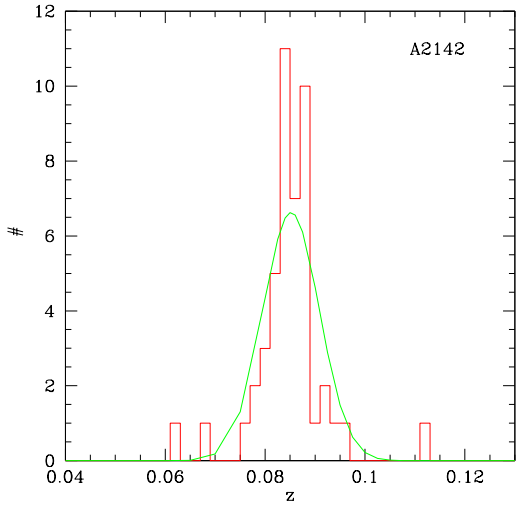

FIG. 1.— Histogram distribution (solid red line) of the best-fit z_X for the 47 regions of Abell 2142 with reliable spectral fit. The green line is the Gaussian with $\sigma_G = \langle\sigma_{\rm tot}\rangle$ centered on $\langle z_X\rangle$.

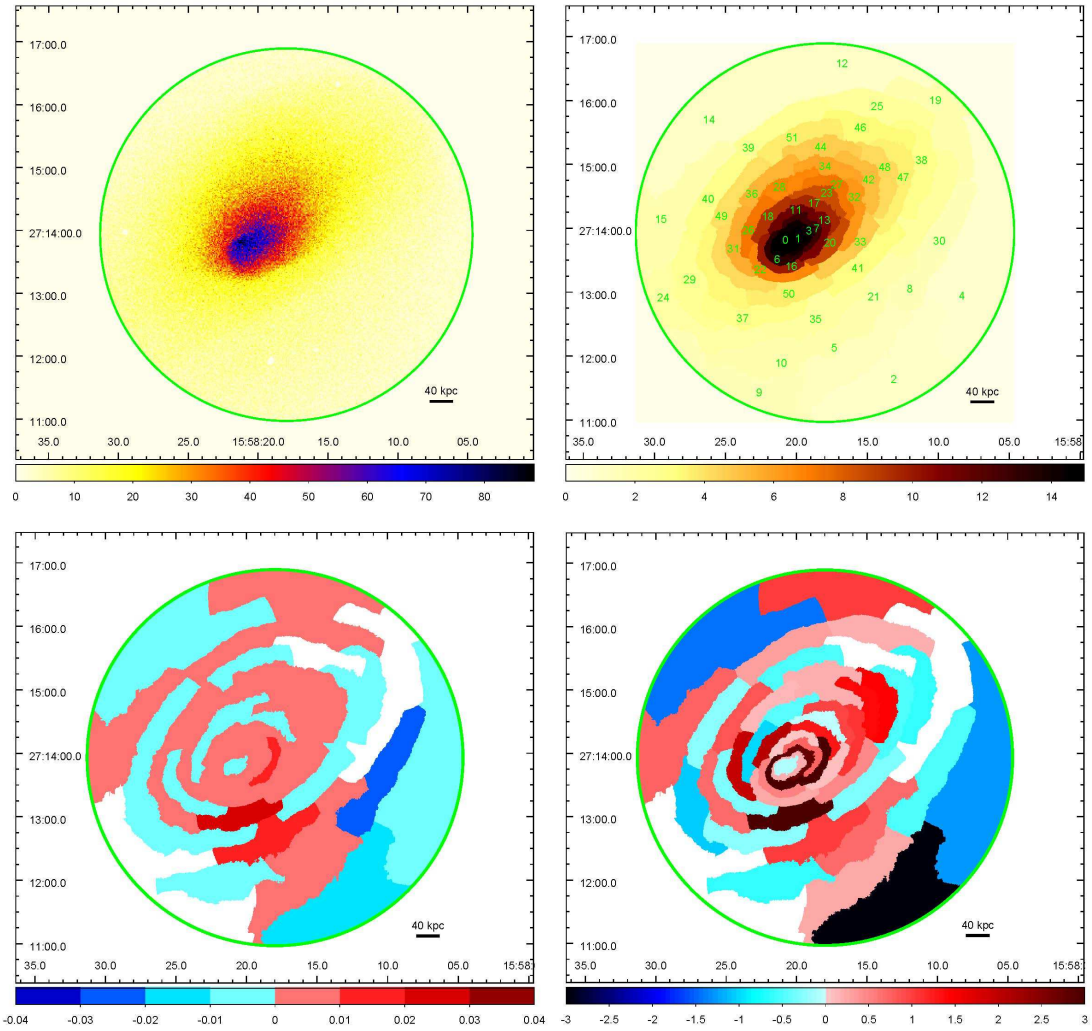

FIG. 2.— Top left panel: surface brightness distribution of Abell 2142 in the 0.5–10 keV band; top right panel: region map; bottom left panel: redshift map; bottom right panel: significance map. White regions do not have a reliable redshift measurement.

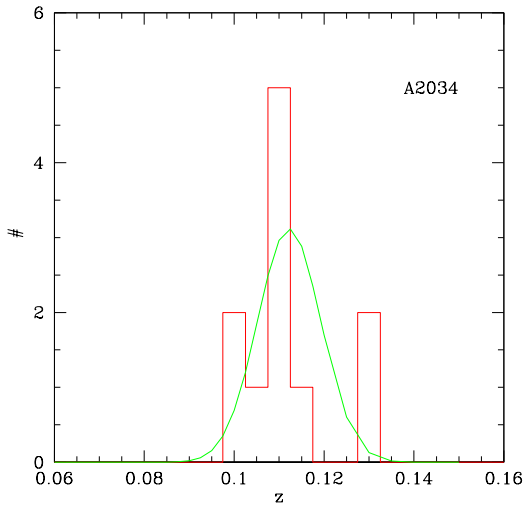

FIG. 3.— Histogram distribution of the best-fit z_X for the 11 regions of Abell 2034 with reliable spectral fit. Lines are as in Figure 1.

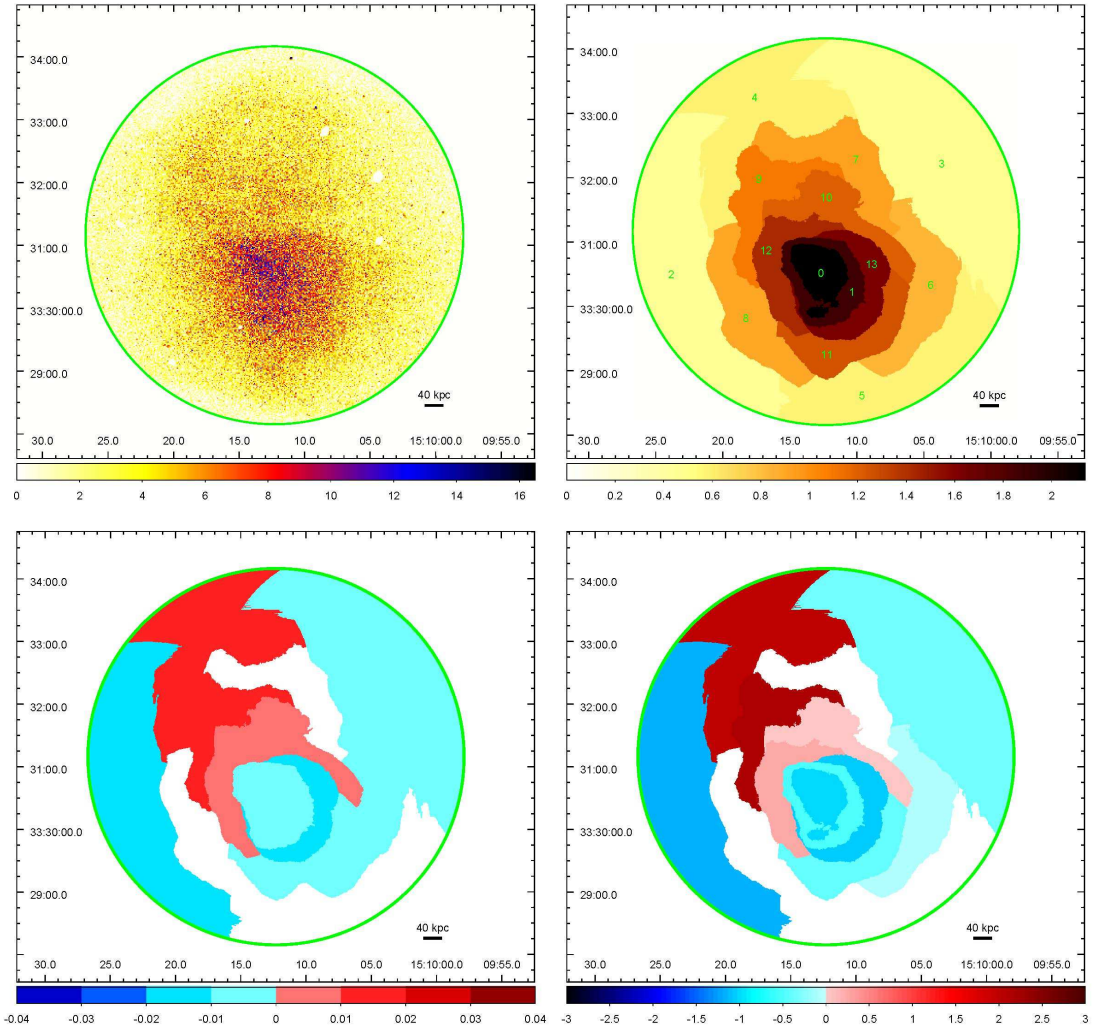

FIG. 4.— Same as Figure 2, but for Abell 2034.

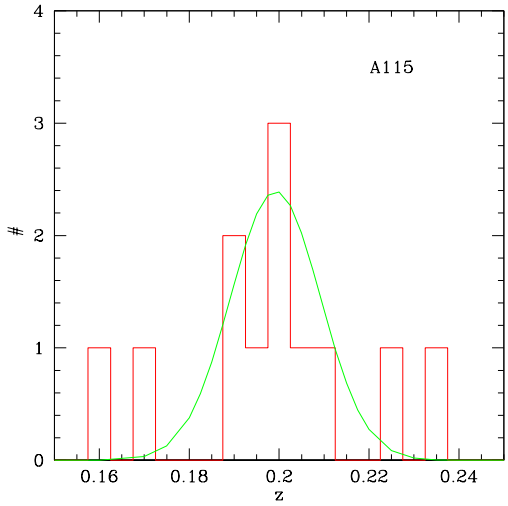

FIG. 5.— Histogram distribution of the best-fit z_X for the 12 regions of Abell 115 with reliable spectral fit. Lines are as in Figure 1.

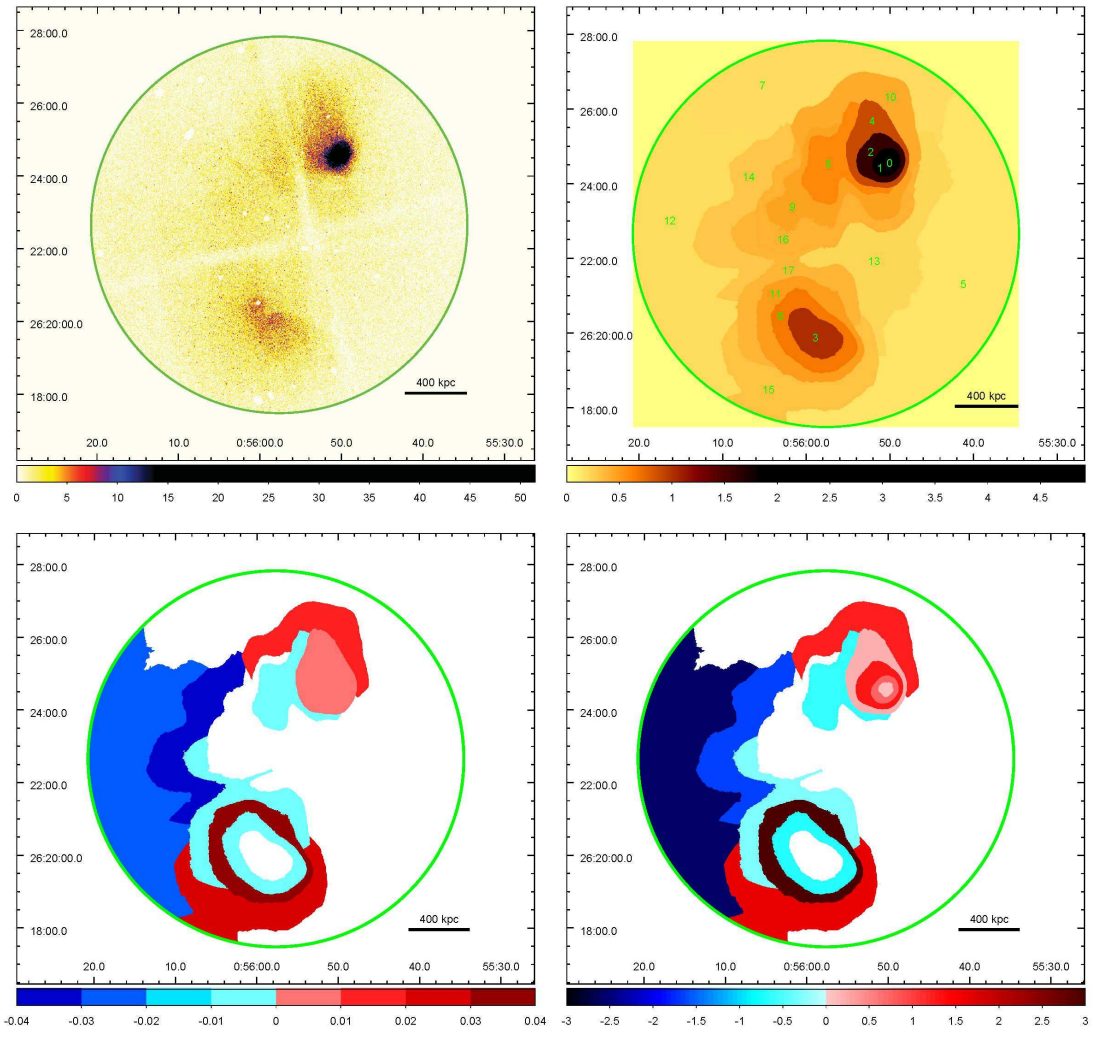

FIG. 6.— Same as Figure 2, but for Abell 115.

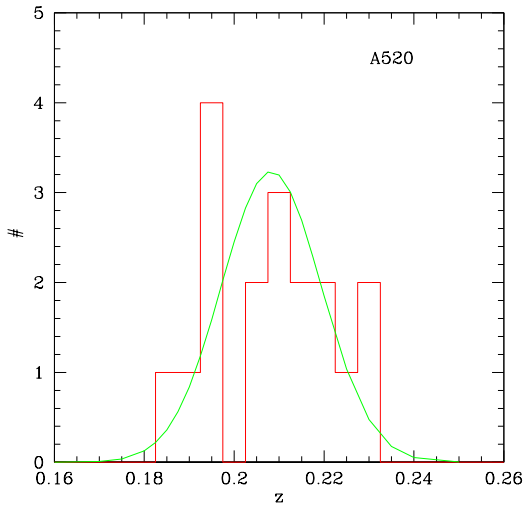

FIG. 7.— Histogram distribution of the best-fit z_X for the 18 regions of Abell 520 with reliable spectral fit. Lines are as in Figure 1.

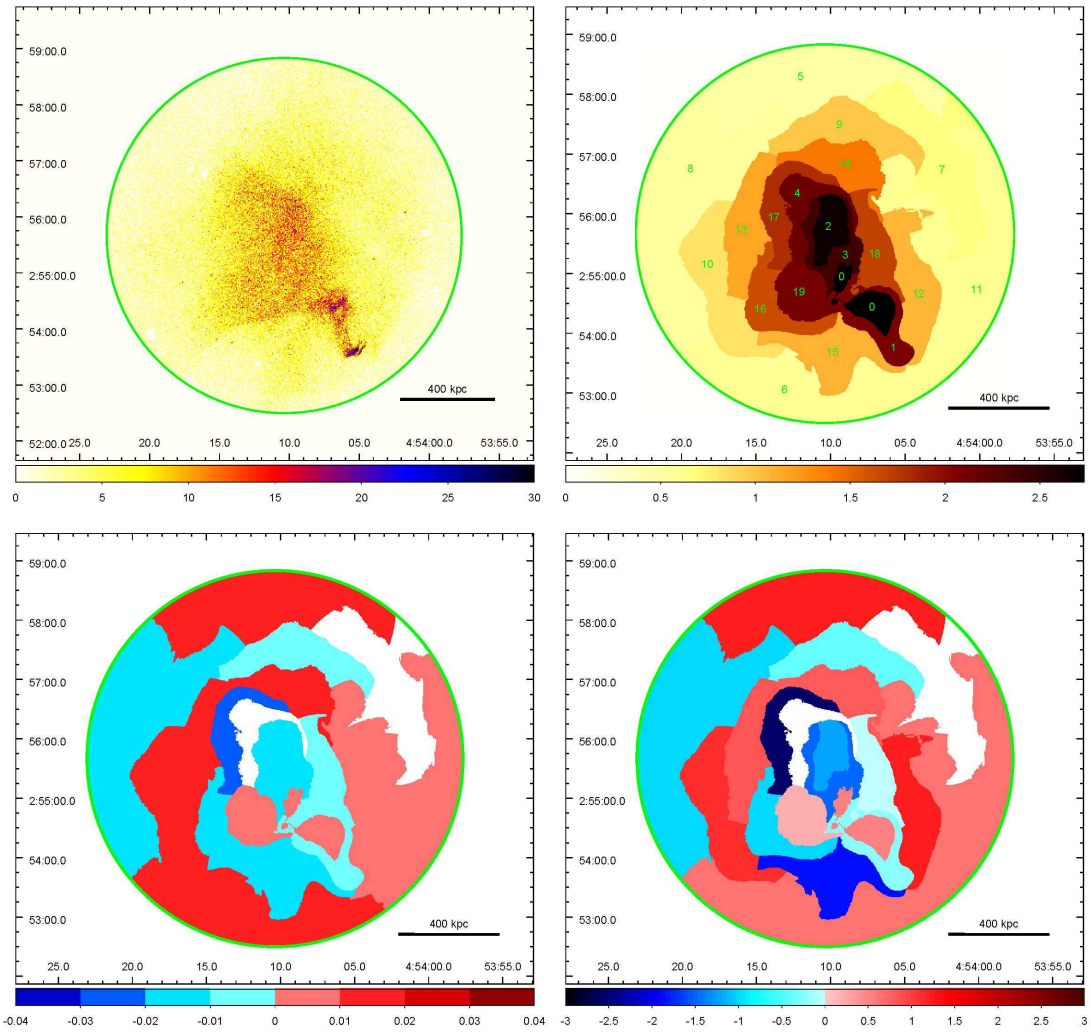

FIG. 8.— Same as Figure 2, but for Abell 520.

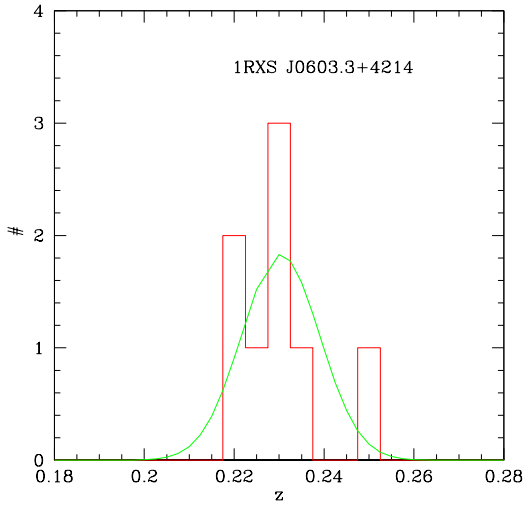

FIG. 9.— Histogram distribution of the best-fit z_X for the 8 regions of 1RXS J0603.3+4214 with reliable spectral fit. Lines are as in Figure 1.

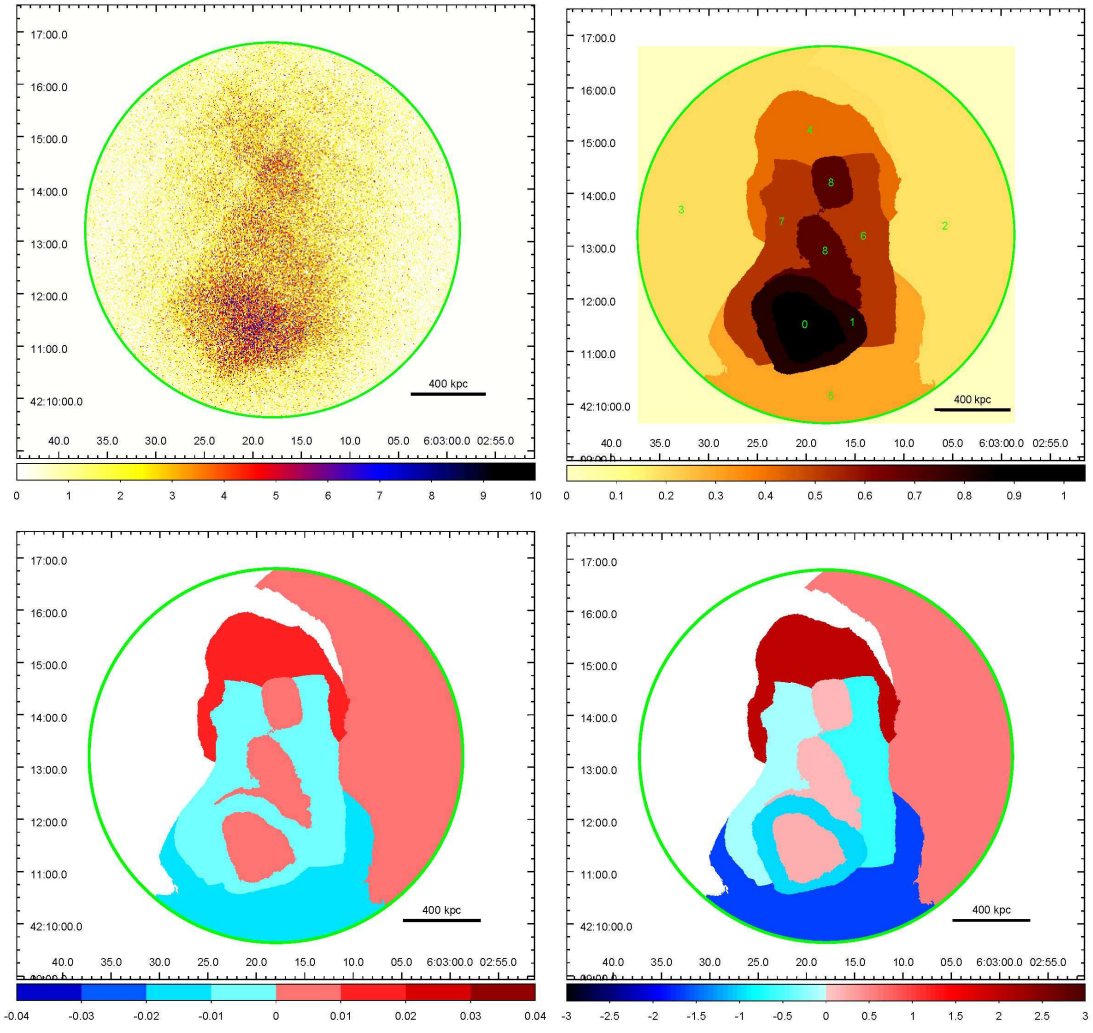

FIG. 10.— Same as Figure 2, but for 1RXS J0603.3+4214.

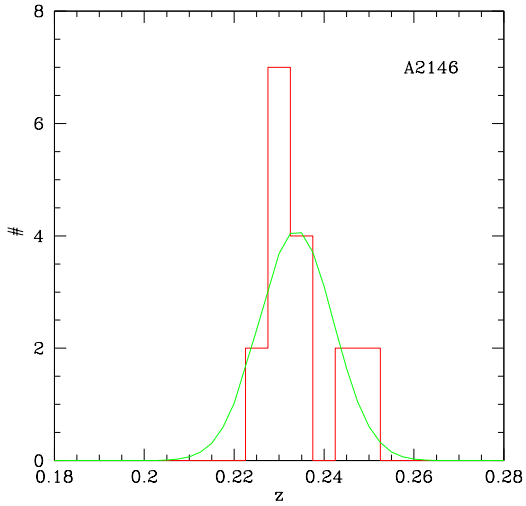

FIG. 11.— Histogram distribution of the best-fit z_X for the 17 regions of A2146 with reliable spectral fit. Lines are as in Figure 1.

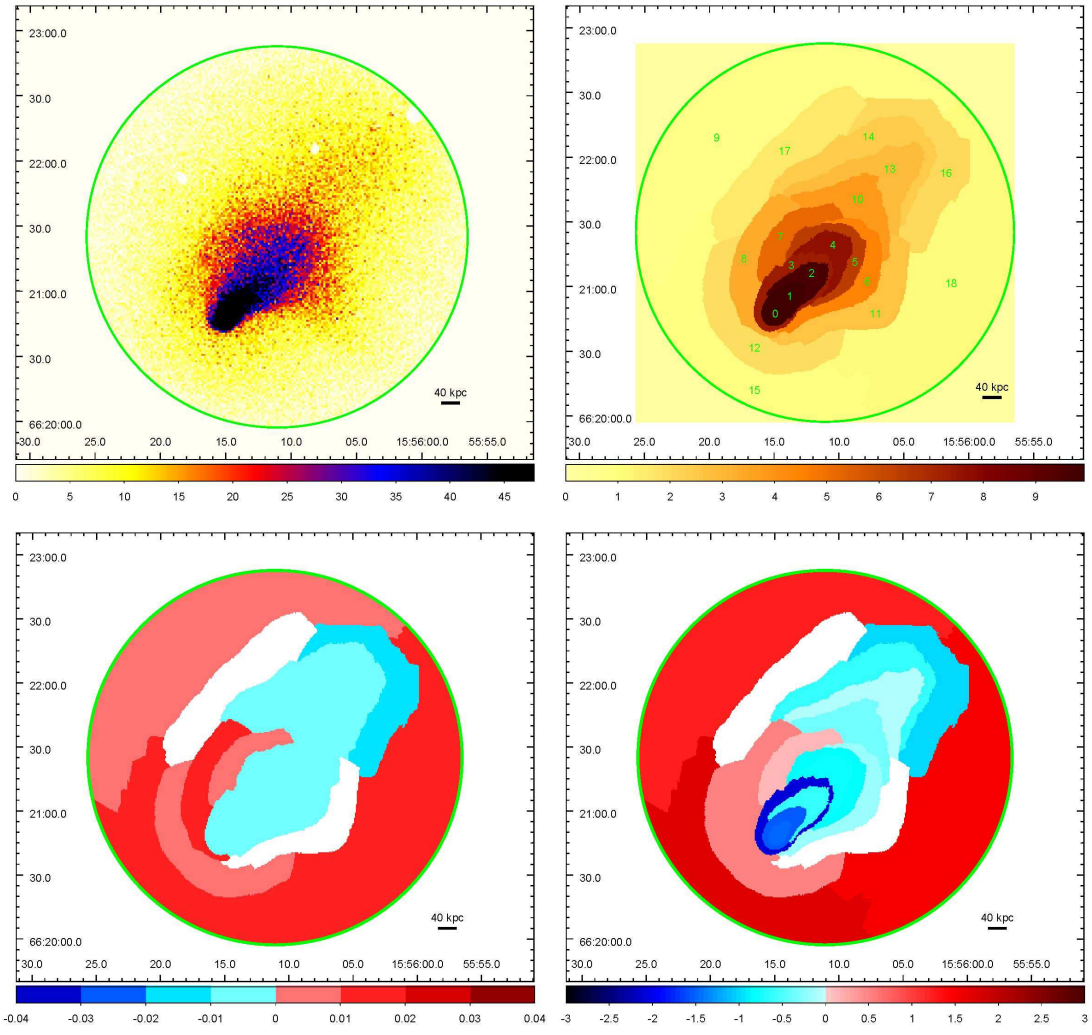

FIG. 12.— Same as Figure 2, but for Abell 2146.

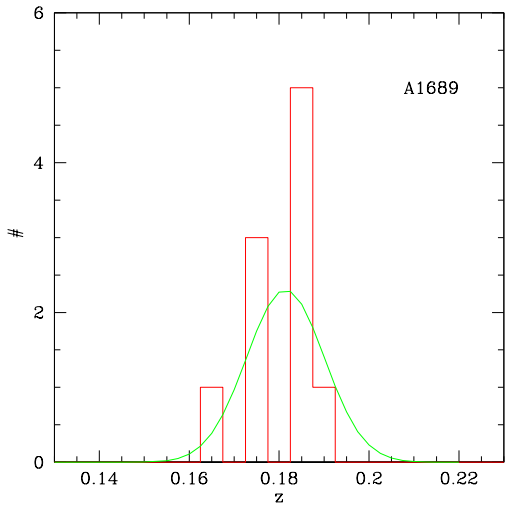

FIG. 13.— Histogram distribution of the best-fit z_X for the 10 regions of A1689 with reliable spectral fit. Lines are as in Figure 1.

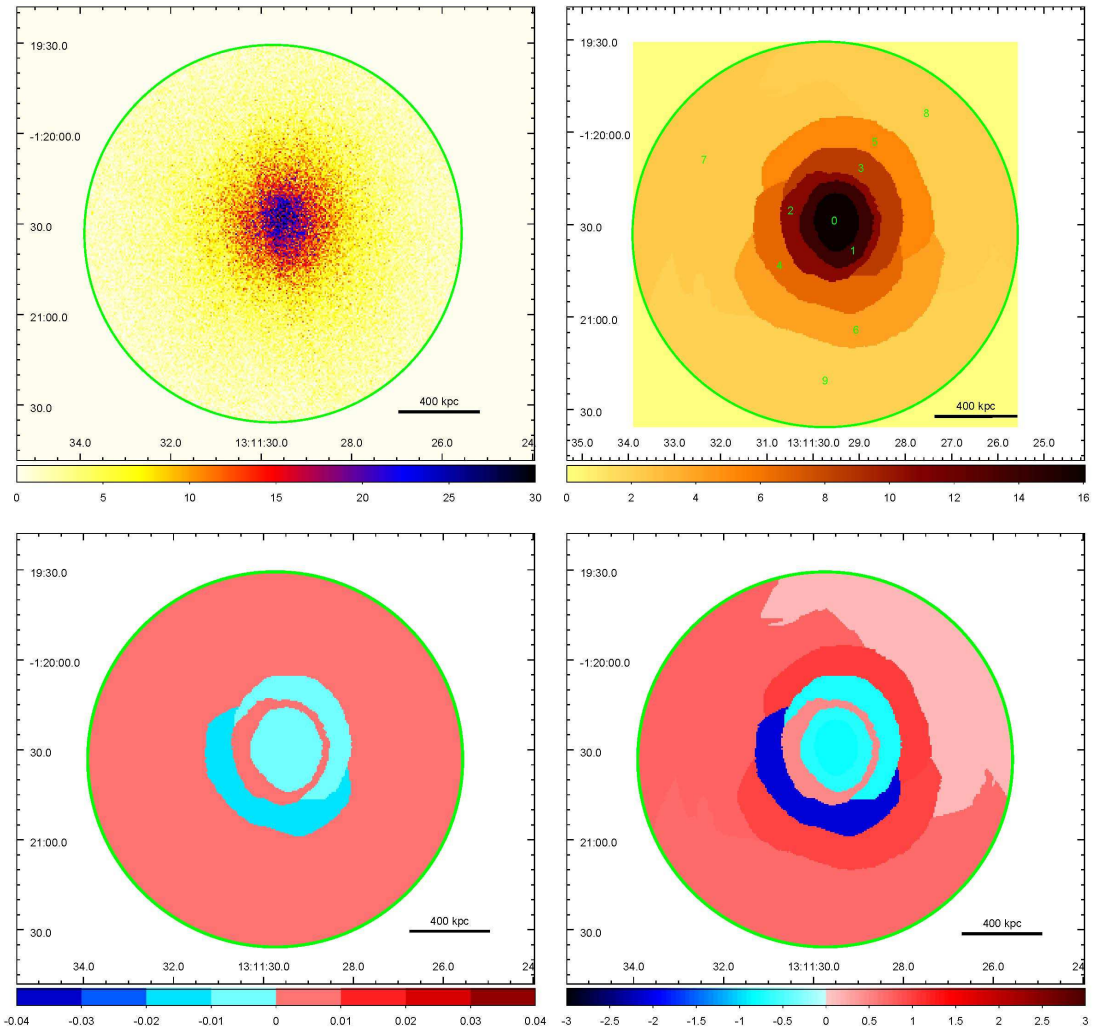

FIG. 14.— Same as Figure 2, but for Abell 1689.

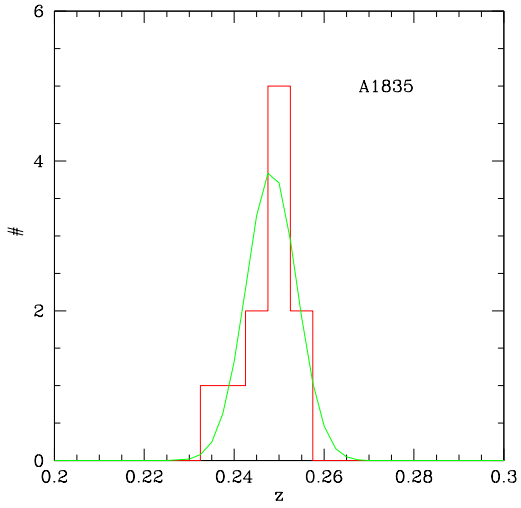

FIG. 15.— Histogram distribution of the best-fit z_X for the 11 regions of A1835 with reliable spectral fit. Lines are as in Figure 1.

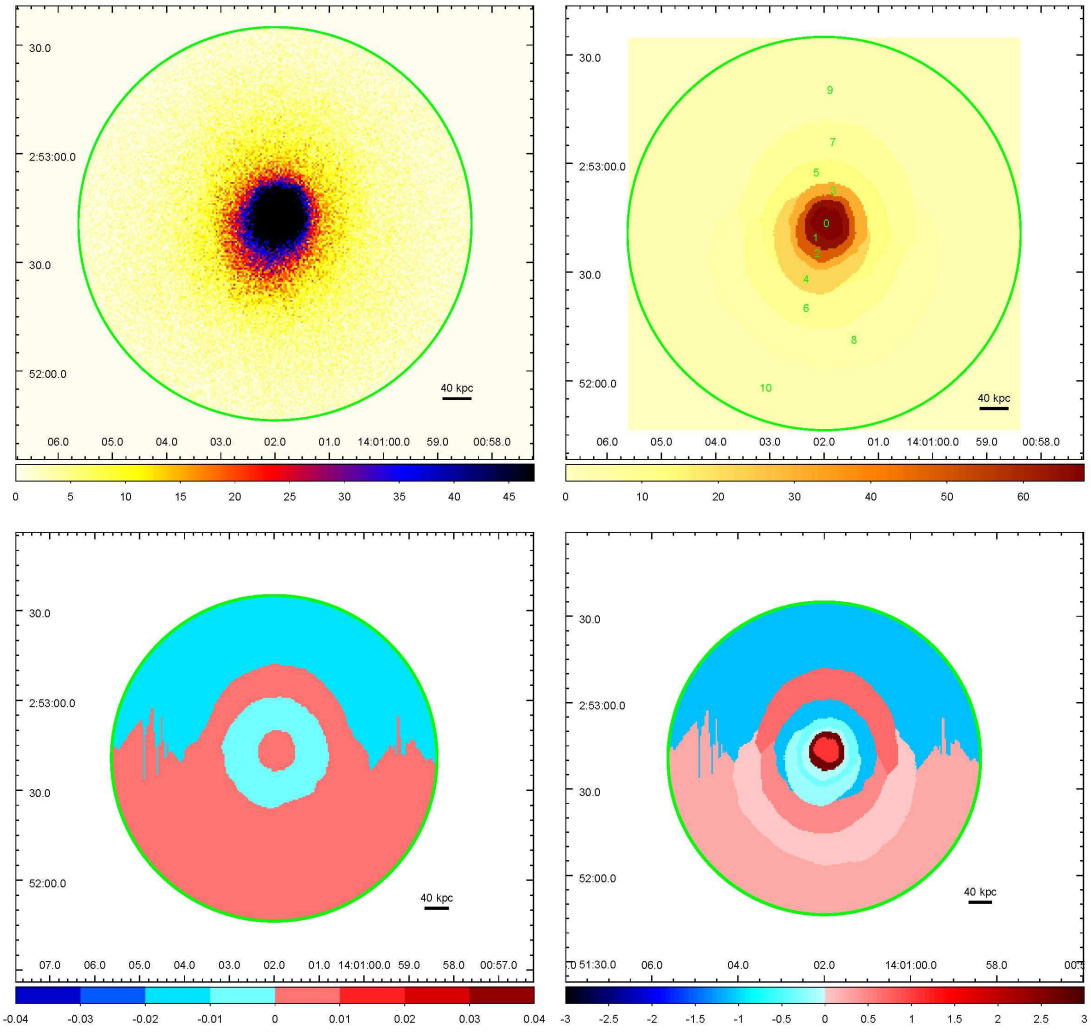

FIG. 16.— Same as Figure 2, but for Abell 1835.

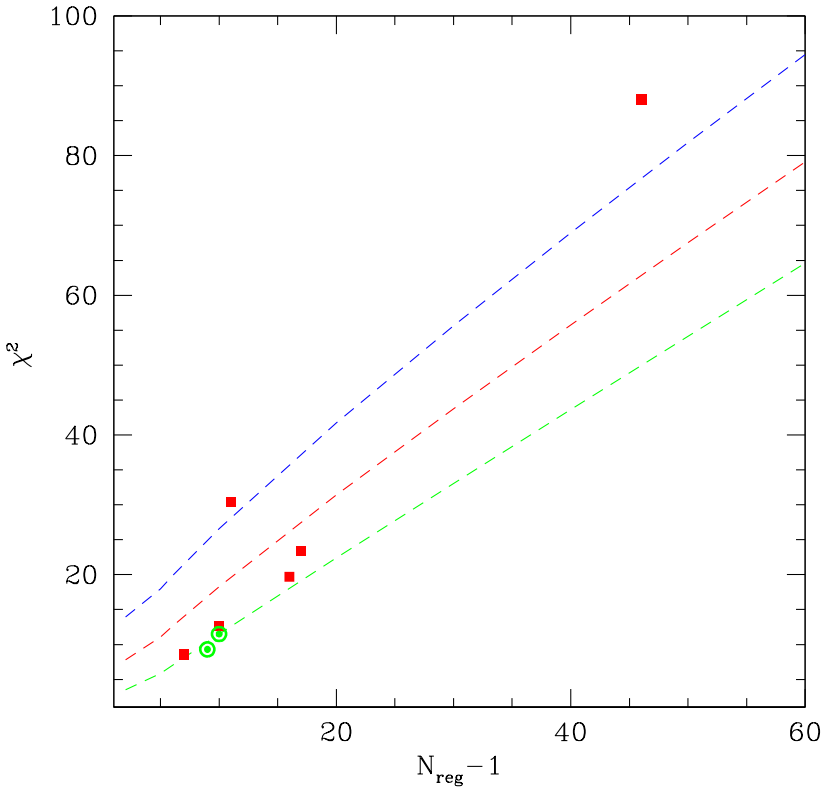

FIG. 17.— Red squares show the χ^2 values versus the degrees of freedom (equal to $N_{\rm reg} - 1$) for merger clusters, while circled green points shows the two relaxed clusters. Dashed lines show the χ^2 values as a function of the degrees of freedom corresponding to the 1, 2, and 3σ confidence levels, from the lowest to the highest.

REFERENCES

Abell, G. O., Corwin, Jr., H. G., & Olowin, R. P. 1989, ApJS, 70, 1
Allen, S. W., Evrard, A. E., & Mantz, A. B. 2011, ARA&A, 49, 409
Arnaud, K. A. 1996, in Astronomical Society of the Pacific Conference Series, Vol. 101, Astronomical Data Analysis Software and Systems V, ed. G. H. Jacoby & J. Barnes, 17
Asplund, M., Grevesse, N., & Sauval, A. J. 2005, in Astronomical Society of the Pacific Conference Series, Vol. 336, Cosmic Abundances as Records of Stellar Evolution and Nucleosynthesis, ed. T. G. Barnes III & F. N. Bash, 25
Barrena, R., Boschin, W., Girardi, M., & Spolaor, M. 2007, A&A, 469, 861
Biffi, V., Dolag, K., & Böhringer, H. 2013, MNRAS, 428, 1395
Bliton, M., Rizza, E., Burns, J. O., Owen, F. N., & Ledlow, M. J. 1998, MNRAS, 301, 609
Brüggen, M., van Weeren, R. J., & Röttgering, H. J. A. 2012, MNRAS, 425, L76
Canning, R. E. A., Russell, H. R., Hatch, N. A., et al. 2012, MNRAS, 420, 2956
Cash, W. 1979, ApJ, 228, 939
Cassano, R., Ettori, S., Brunetti, G., et al. 2013, ApJ, 777, 141
Cuciti, V., Cassano, R., Brunetti, G., et al. 2015, A&A, 580, A97
Diaferio, A. 1999, MNRAS, 309, 610
Diaferio, A., Geller, M. J., & Rines, K. J. 2005, ApJL, 628, L97
Dupke, R. A., & Bregman, J. N. 2001a, ApJ, 562, 266
—. 2001b, ApJ, 547, 705
—. 2005, ApJS, 161, 224
—. 2006, ApJ, 639, 781
Dupke, R. A., Mirabal, N., Bregman, J. N., & Evrard, A. E. 2007, ApJ, 668, 781
Forman, W., Bechtold, J., Blair, W., et al. 1981, ApJL, 243, L133
Giovannini, G., Bonafede, A., Feretti, L., et al. 2009, A&A, 507, 1257
Giovannini, G., Tordi, M., & Feretti, L. 1999, NewA, 4, 141
Girardi, M., Barrena, R., Boschin, W., & Ellingson, E. 2008, A&A, 491, 379
Girardi, M., Aguerri, J. A. L., De Grandi, S., et al. 2014, A&A, 565, A115
Govoni, F., Feretti, L., Giovannini, G., et al. 2001, A&A, 376, 803
Gutierrez, K., & Krawczynski, H. 2005, ApJ, 619, 161
Henry, J. P., & Briel, U. G. 1996, ApJ, 472, 137
Hiroi, K., Ueda, Y., Hayashida, M., et al. 2013, ApJS, 207, 36
Kalberla, P. M. W., Burton, W. B., Hartmann, D., et al. 2005, A&A, 440, 775
Kempner, J. C., & Sarazin, C. L. 2001, ApJ, 548, 639
Kempner, J. C., Sarazin, C. L., & Markevitch, M. 2003, ApJ, 593, 291
Komatsu, E., Smith, K. M., Dunkley, J., et al. 2011, ApJS, 192, 18
Liedahl, D. A., Osterheld, A. L., & Goldstein, W. H. 1995, ApJL, 438, L115
Liu, A., Yu, H., Tozzi, P., & Zhu, Z.-H. 2015, ApJ, 809, 27
Lyons, L. 2008, Ann. Appl. Stat., 2, 887
Mahdavi, A., Hoekstra, H., Babul, A., Balam, D. D., & Capak, P. L. 2007, ApJ, 668, 806
Mann, A. W., & Ebeling, H. 2012, MNRAS, 420, 2120
Markevitch, M., Gonzalez, A. H., David, L., et al. 2002, ApJL, 567, L27
Markevitch, M., Govoni, F., Brunetti, G., & Jerius, D. 2005, ApJ, 627, 733
Markevitch, M., Ponman, T. J., Nulsen, P. E. J., et al. 2000, ApJ, 541, 542
Mazzotta, P., Rasia, E., Moscardini, L., & Tormen, G. 2004, MNRAS, 354, 10
Mewe, R., Gronenschild, E. H. B. M., & van den Oord, G. H. J. 1985, A&AS, 62, 197
Mewe, R., Lemen, J. R., & van den Oord, G. H. J. 1986, A&AS, 65, 511
Mitchell, R. J., Culhane, J. L., Davison, P. J. N., & Ives, J. C. 1976, MNRAS, 175, 29P
Muriel, H., & Coenda, V. 2014, A&A, 564, A85
Nagai, D., Kravtsov, A. V., & Kosowsky, A. 2003, ApJ, 587, 524
Nagai, D., Lau, E. T., Avestruz, C., Nelson, K., & Rudd, D. H. 2013, ApJ, 777, 137
Nelson, K., Lau, E. T., Nagai, D., Rudd, D. H., & Yu, L. 2014, ApJ, 782, 107
Nousek, J. A., & Shue, D. R. 1989, ApJ, 342, 1207
Oegerle, W. R., Hill, J. M., & Fitchett, M. J. 1995, AJ, 110, 32
Ogrean, G. A., Brüggen, M., van Weeren, R. J., et al. 2013, MNRAS, 433, 812
Ota, N., & Yoshida, H. 2015, ArXiv e-prints, arXiv:1511.07904
Owers, M. S., Nulsen, P. E. J., Couch, W. J., et al. 2014, ApJ, 780, 163
Parekh, V., van der Heyden, K., Ferrari, C., Angus, G., & Holwerda, B. 2015, A&A, 575, A127
Piffaretti, R., Arnaud, M., Pratt, G. W., Pointecouteau, E., & Melin, J.-B. 2011, A&A, 534, A109
Pinto, C., Sanders, J. S., Werner, N., et al. 2015, A&A, 575, A38
Proust, D., Cuevas, H., Capelato, H. V., et al. 2000, A&A, 355, 443
Rosati, P., Tozzi, P., Ettori, S., et al. 2004, AJ, 127, 230
Rosati, P., Tozzi, P., Gobat, R., et al. 2009, A&A, 508, 583
Russell, H. R., Sanders, J. S., Fabian, A. C., et al. 2010, MNRAS, 406, 1721
Russell, H. R., van Weeren, R. J., Edge, A. C., et al. 2011, MNRAS, 417, L1
Sanders, J. S. 2006, MNRAS, 371, 829
Sanders, J. S., Fabian, A. C., Smith, R. K., & Peterson, J. R. 2010, MNRAS, 402, L11
Sato, K., Matsushita, K., Ishisaki, Y., et al. 2008, PASJ, 60, 333
Sato, T., Matsushita, K., Ota, N., et al. 2011, PASJ, 63, 991
Serra, A. L., & Diaferio, A. 2013, ApJ, 768, 116
Shibata, R., Honda, H., Ishida, M., Ohashi, T., & Yamashita, K. 1999, ApJ, 524, 603
Stanford, S. A., Eisenhardt, P. R., Brodwin, M., et al. 2005, ApJL, 634, L129
Sugawara, C., Takizawa, M., & Nakazawa, K. 2009, PASJ, 61, 1293
Takahashi, T., Mitsuda, K., Kelley, R., et al. 2014, ArXiv e-prints, arXiv:1412.2351
Tamura, T., Hayashida, K., Ueda, S., & Nagai, M. 2011, PASJ, 63, 1009
Tamura, T., Yamasaki, N. Y., Iizuka, R., et al. 2014, ApJ, 782, 38
Tozzi, P., Santos, J. S., Nonino, M., et al. 2013, A&A, 551, A45
Tozzi, P., Santos, J. S., Jee, M. J., et al. 2015, ApJ, 799, 93
van Weeren, R. J., Brüggen, M., Röttgering, H. J. A., et al. 2011, A&A, 533, A35
van Weeren, R. J., Röttgering, H. J. A., Intema, H. T., et al. 2012, A&A, 546, A124
Wilms, J., Allen, A., & McCray, R. 2000, ApJ, 542, 914
Yu, H., Serra, A. L., Diaferio, A., & Baldi, M. 2015, ApJ, 810, 37
Yu, H., Tozzi, P., Borgani, S., Rosati, P., & Zhu, Z.-H. 2011, A&A, 529, A65
Zhuravleva, I., Churazov, E., Schekochihin, A. A., et al. 2014, Nature, 515, 85

APPENDIX

SPECTRAL ANALYSIS RESULTS OF THE CLUSTERS

For each cluster analyzed in this work we report the best fit redshift z_X along with the statistical, systematic and total error in all the selected regions with reliable spectral fit.

TABLE 5
SPECTRAL ANALYSIS RESULTS OF ABELL 2142.

Region	z	$\sigma_{\mathrm{stat_b}}$	$\sigma_{\mathrm{stat_u}}$	$\sigma_{\mathrm{syst_b}}$	$\sigma_{\mathrm{syst_u}}$	$\sigma_{\mathrm{tot_b}}$	$\sigma_{\mathrm{tot_u}}$
0	0.0839	-0.0030	0.0033	-0.0009	0.0002	-0.0031	0.0034
1	0.0847	-0.0021	0.0026	-0.0007	0.0013	-0.0022	0.0029
2	0.0674	-0.0048	0.0050	-0.0014	0.0005	-0.0051	0.0050
3	0.0881	-0.0013	0.0029	-0.0001	0.0018	-0.0014	0.0034
4	0.0762	-0.0064	0.0061	-0.0040	0.0001	-0.0076	0.0061
5	0.0863	-0.0065	0.0058	-0.0054	0.0026	-0.0084	0.0063
6	0.0917	-0.0022	0.0024	-0.0001	0.0013	-0.0022	0.0027
7	0.0866	-0.0031	0.0032	-0.0001	0.0015	-0.0031	0.0035
8	0.0612	-0.0064	0.0075	-0.0001	0.0455	-0.0064	0.0461
10	0.0808	-0.0039	0.0039	-0.0001	0.0040	-0.0039	0.0055
11	0.0843	-0.0030	0.0032	-0.0001	0.0020	-0.0030	0.0038
12	0.0885	-0.0042	0.0098	-0.0001	0.0010	-0.0042	0.0099
13	0.0946	-0.0034	0.0036	-0.0001	0.0014	-0.0034	0.0039
14	0.0787	-0.0043	0.0036	-0.0007	0.0013	-0.0044	0.0039
15	0.0874	-0.0043	0.0036	-0.0001	0.0016	-0.0043	0.0040
16	0.0860	-0.0036	0.0038	-0.0001	0.0030	-0.0036	0.0049
17	0.0888	-0.0029	0.0031	-0.0020	0.0001	-0.0035	0.0031
18	0.0908	-0.0032	0.0024	-0.0001	0.0013	-0.0032	0.0027
20	0.0844	-0.0029	0.0028	-0.0004	0.0015	-0.0030	0.0031
21	0.0885	-0.0061	0.0083	-0.0015	0.0025	-0.0063	0.0087
22	0.0852	-0.0033	0.0033	-0.0012	0.0020	-0.0036	0.0039
23	0.0841	-0.0037	0.0038	-0.0001	0.0020	-0.0037	0.0043
25	0.0848	-0.0028	0.0027	-0.0001	0.0022	-0.0028	0.0034
26	0.0811	-0.0027	0.0029	-0.0010	0.0010	-0.0028	0.0031
27	0.0882	-0.0040	0.0038	-0.0010	0.0001	-0.0041	0.0038
28	0.0831	-0.0029	0.0024	-0.0010	0.0001	-0.0031	0.0024
29	0.0777	-0.0044	0.0045	-0.0017	0.0043	-0.0047	0.0062
31	0.0914	-0.0036	0.0040	-0.0001	0.0025	-0.0036	0.0047
32	0.0869	-0.0023	0.0022	-0.0010	0.0010	-0.0025	0.0024
33	0.0878	-0.0071	0.0100	-0.0028	0.0132	-0.0076	0.0166
34	0.0847	-0.0027	0.0027	-0.0007	0.0007	-0.0028	0.0028
35	0.0966	-0.0083	0.0058	-0.0087	0.0043	-0.0120	0.0072
36	0.0846	-0.0027	0.0026	-0.0006	0.0024	-0.0028	0.0035
37	0.0821	-0.0053	0.0050	-0.0010	0.0060	-0.0054	0.0078
38	0.0808	-0.0045	0.0046	-0.0013	0.0032	-0.0047	0.0056
39	0.0853	-0.0034	0.0035	-0.0001	0.0016	-0.0034	0.0038
40	0.0832	-0.0033	0.0035	-0.0007	0.0023	-0.0034	0.0042
41	0.0826	-0.0055	0.0041	-0.0001	0.0034	-0.0055	0.0053
42	0.0876	-0.0024	0.0027	-0.0001	0.0030	-0.0024	0.0040
43	0.0820	-0.0049	0.0053	-0.0001	0.0050	-0.0049	0.0073
44	0.0848	-0.0027	0.0023	-0.0008	0.0012	-0.0028	0.0026
45	0.0884	-0.0054	0.0051	-0.0024	0.0036	-0.0059	0.0062
47	0.0823	-0.0037	0.0036	-0.0001	0.0010	-0.0037	0.0037
48	0.0885	-0.0029	0.0031	-0.0001	0.0010	-0.0029	0.0033
49	0.0866	-0.0028	0.0030	-0.0001	0.0014	-0.0028	0.0033
50	0.1124	-0.0052	0.0063	-0.0025	0.0045	-0.0057	0.0077
51	0.0881	-0.0049	0.0044	-0.0001	0.0052	-0.0049	0.0068 [a]

[a]Column 1: region number; Column 2: best-fit redshift z_{X} obtained fitting the 2.0–10 keV energy range; Columns 3 & 4: lower and upper 1σ error bars from fit statistics; Columns 5 & 6: lower and upper 1σ error bars from systematics associated to the ICM temperature structure; Columns 7& 8: total lower and upper 1σ error bars computed as $\sigma_{\mathrm{tot}} = \sqrt{\sigma^2_{\mathrm{stat}} + \sigma^2_{\mathrm{syst}}}$.

TABLE 6
SPECTRAL ANALYSIS RESULTS OF ABELL 2034.

Region	z	$\sigma_{\mathrm{stat_b}}$	$\sigma_{\mathrm{stat_u}}$	$\sigma_{\mathrm{syst_b}}$	$\sigma_{\mathrm{syst_u}}$	$\sigma_{\mathrm{tot_b}}$	$\sigma_{\mathrm{tot_u}}$
0	0.1056	-0.0057	0.0056	-0.0001	0.0033	-0.0057	0.0065
1	0.1085	-0.006	0.0068	-0.0016	0.0014	-0.0062	0.0069
2	0.1004	-0.0062	0.0088	-0.0001	0.0054	-0.0062	0.0103
3	0.1089	-0.0074	0.008	-0.0017	0.0053	-0.0075	0.0095
4	0.1318	-0.0093	0.0076	-0.0035	0.0001	-0.0099	0.0076
6	0.1116	-0.0038	0.0055	-0.0001	0.0018	-0.0038	0.0057
9	0.1301	-0.0067	0.0058	-0.0049	0.0001	-0.0083	0.0058
10	0.1124	-0.0055	0.0059	-0.0018	0.0001	-0.0057	0.0059
11	0.1099	-0.0077	0.0061	-0.0051	0.0001	-0.0092	0.0061
12	0.1142	-0.0075	0.0102	-0.0035	0.0018	-0.0082	0.0103
13	0.1011	-0.0068	0.0095	-0.0001	0.0040	-0.0068	0.0103 [a]

[a]The columns are the same as in Table 5.

TABLE 7
SPECTRAL ANALYSIS RESULTS OF ABELL 115.

Region	z	σ_{stat_b}	σ_{stat_u}	σ_{syst_b}	σ_{syst_u}	σ_{tot_b}	σ_{tot_u}
0	0.1980	-0.0019	0.0036	-0.0000	0.0025	-0.0019	0.0044
1	0.1998	-0.0027	0.0028	-0.0000	0.0002	-0.0027	0.0028
2	0.2026	-0.0036	0.0039	-0.0000	0.0037	-0.0036	0.0053
4	0.1988	-0.0051	0.0042	-0.0000	0.0061	-0.0051	0.0074
6	0.1922	-0.0067	0.0083	-0.0032	0.0018	-0.0074	0.0085
8	0.1897	-0.0124	0.0123	-0.0037	0.0053	-0.0129	0.0134
10	0.2090	-0.0082	0.0086	-0.0040	0.0040	-0.0091	0.0095
11	0.2367	-0.0060	0.0048	-0.0087	0.0000	-0.0106	0.0048
12	0.1679	-0.0094	0.0113	-0.0049	0.0020	-0.0106	0.0115
14	0.1591	-0.0064	0.0094	-0.0000	0.0210	-0.0064	0.0230
15	0.2263	-0.0177	0.0107	-0.0000	0.0000	-0.0177	0.0107
17	0.1943	-0.0069	0.0074	-0.0038	0.0107	-0.0079	0.0130 [a]

[a] The columns are the same as in Table 5.

TABLE 8
SPECTRAL ANALYSIS RESULTS OF ABELL 520.

Region	z	σ_{stat_b}	σ_{stat_u}	σ_{syst_b}	σ_{syst_u}	σ_{tot_b}	σ_{tot_u}
0	0.2102	-0.0037	0.0065	-0.0001	0.0021	-0.0037	0.0068
1	0.2069	-0.0047	0.0043	-0.0001	0.0027	-0.0047	0.0050
2	0.1933	-0.0085	0.0096	-0.0001	0.0074	-0.0085	0.0121
3	0.1962	-0.0075	0.0076	-0.0001	0.0024	-0.0075	0.0079
5	0.2276	-0.0155	0.0147	-0.0025	0.0049	-0.0157	0.0154
6	0.2207	-0.0146	0.0079	-0.0122	0.0001	-0.0190	0.0079
8	0.1937	-0.0128	0.0133	-0.0018	0.0056	-0.0129	0.0144
9	0.2048	-0.0087	0.0075	-0.0006	0.0027	-0.0087	0.0079
10	0.2271	-0.0164	0.0138	-0.0039	0.0001	-0.0168	0.0138
11	0.2152	-0.0106	0.0096	-0.0012	0.0058	-0.0106	0.0112
12	0.2138	-0.0046	0.0053	-0.0001	0.0044	-0.0046	0.0068
13	0.2282	-0.0149	0.0126	-0.0175	0.0006	-0.0229	0.0126
14	0.2217	-0.0153	0.0166	-0.0066	0.0001	-0.0166	0.0166
15	0.1921	-0.0088	0.0085	-0.0083	0.0001	-0.0120	0.0085
16	0.195	-0.0124	0.0131	-0.0081	0.0001	-0.0148	0.0131
17	0.1837	-0.0085	0.0086	-0.0001	0.0038	-0.0085	0.0094
18	0.208	-0.0102	0.0068	-0.0057	0.0005	-0.0116	0.0068
19	0.2104	-0.0099	0.0093	-0.0001	0.0114	-0.0099	0.0147 [a]

[a]The columns are the same as in Table 5.

TABLE 9
SPECTRAL ANALYSIS RESULTS OF 1RXS J0603.3+4214.

Region	z	σ_{stat_b}	σ_{stat_u}	σ_{syst_b}	σ_{syst_u}	σ_{tot_b}	σ_{tot_u}
0	0.2317	-0.0062	0.0065	-0.0030	0.0004	-0.0068	0.0065
1	0.2206	-0.0069	0.0072	-0.0021	0.0065	-0.0072	0.0097
2	0.2347	-0.0075	0.0119	-0.0008	0.0071	-0.0075	0.0138
4	0.2493	-0.0067	0.0091	-0.0069	0.0001	-0.0096	0.0091
5	0.2198	-0.0070	0.0063	-0.0045	0.0001	-0.0083	0.0063
6	0.2254	-0.0108	0.0078	-0.0055	0.0001	-0.0121	0.0078
7	0.2294	-0.0094	0.0066	-0.0044	0.0021	-0.0103	0.0069
8	0.2316	-0.0091	0.0075	-0.0001	0.0042	-0.0091	0.0085 [a]

[a]The columns are the same as in Table 5.

TABLE 10
SPECTRAL ANALYSIS RESULTS OF ABELL 2146.

Region	z	σ_{stat_b}	σ_{stat_u}	σ_{syst_b}	σ_{syst_u}	σ_{tot_b}	σ_{tot_u}
0	0.2292	-0.0045	0.00312787	-0.0000	0.0000	-0.0045	0.0031
1	0.2282	-0.0035	0.00311993	-0.0017	0.0018	-0.0039	0.0036
2	0.2277	-0.0038	0.00571345	-0.0000	0.0083	-0.0038	0.0100
3	0.2282	-0.0051	0.0026654	-0.0027	0.0000	-0.0057	0.0027
4	0.2294	-0.0037	0.00436681	-0.0000	0.0036	-0.0037	0.0057
5	0.2276	-0.0065	0.00615287	-0.0001	0.0044	-0.0065	0.0076
6	0.2325	-0.0074	0.00676923	-0.0055	0.0000	-0.0092	0.0068
7	0.2354	-0.0060	0.00619396	-0.0114	0.0000	-0.0129	0.0062
8	0.2473	-0.0125	0.0069235	-0.0223	0.0000	-0.0255	0.0069
9	0.2436	-0.0072	0.0066689	-0.0036	0.0000	-0.0080	0.0067
10	0.2277	-0.0083	0.00881529	-0.0000	0.0140	-0.0083	0.0165
12	0.2372	-0.0062	0.00682796	-0.0010	0.0010	-0.0063	0.0069
13	0.2326	-0.0088	0.00909447	-0.0025	0.0074	-0.0091	0.0117
14	0.2256	-0.0077	0.00950732	-0.0025	0.0086	-0.0081	0.0128
15	0.2495	-0.0089	0.00691656	-0.0015	0.0000	-0.0090	0.0069
16	0.2226	-0.0114	0.0110643	-0.0060	0.0000	-0.0129	0.0110
18	0.2505	-0.0075	0.00798135	-0.0080	0.0000	-0.0110	0.0080 [a]

[a]The columns are the same as in Table 5.

TABLE 11
SPECTRAL ANALYSIS RESULTS OF ABELL 1689.

Region	z	σ_{stat_b}	σ_{stat_u}	σ_{syst_b}	σ_{syst_u}	σ_{tot_b}	σ_{tot_u}
0	0.1767	-0.0061	0.0048	-0.0001	0.0037	-0.0061	0.0060
1	0.1774	-0.0047	0.0061	-0.0014	0.0001	-0.0049	0.0061
2	0.1864	-0.0103	0.0109	-0.0001	0.0066	-0.0103	0.0127
3	0.1774	-0.0065	0.0049	-0.0019	0.002	-0.0067	0.0052
4	0.1675	-0.0074	0.0066	-0.0019	0.0001	-0.0076	0.0066
5	0.1859	-0.0045	0.0038	-0.0001	0.0016	-0.0045	0.0041
6	0.1895	-0.0084	0.0087	-0.0001	0.0385	-0.0084	0.0394
7	0.1859	-0.006	0.0078	-0.0001	0.0041	-0.0060	0.0088
8	0.1826	-0.0087	0.0073	-0.0001	0.005	-0.0087	0.0088
9	0.1847	-0.0047	0.0071	-0.0001	0.0031	-0.0047	0.0077 [a]

[a]The columns are the same as in Table 5.

TABLE 12
SPECTRAL ANALYSIS RESULTS OF ABELL 1835.

Region	z	σ_{stat_b}	σ_{stat_u}	σ_{syst_b}	σ_{syst_u}	σ_{tot_b}	σ_{tot_u}
0	0.2524	-0.0031	0.0041	-0.0024	0.0001	-0.0039	0.0041
1	0.2547	-0.0024	0.003	-0.0001	0.0025	-0.0024	0.0039
2	0.2478	-0.003	0.0052	-0.0001	0.0021	-0.0030	0.0056
3	0.2474	-0.003	0.0027	-0.002	0.0003	-0.0036	0.0027
4	0.2472	-0.0048	0.006	-0.002	0.0018	-0.0052	0.0062
5	0.2408	-0.0028	0.0045	-0.0001	0.0052	-0.0028	0.0068
6	0.2538	-0.01	0.0065	-0.0057	0.0016	-0.0115	0.0066
7	0.2519	-0.0046	0.0064	-0.0028	0.0001	-0.0053	0.0064
8	0.2486	-0.006	0.0052	-0.0001	0.0046	-0.0060	0.0069
9	0.2372	-0.0065	0.0073	-0.0002	0.007	-0.0065	0.0101
10	0.2496	-0.0068	0.0078	-0.0019	0.0023	-0.0070	0.0081 [a]

[a]The columns are the same as in Table 5.